

RD-A155 948

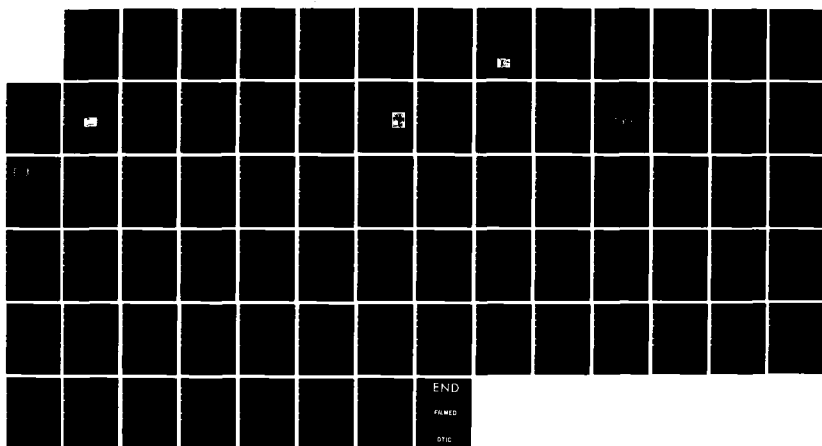
APPLIED LASERS (SELECTED ARTICLES)(U) FOREIGN
TECHNOLOGY DIV WRIGHT-PATTERSON AFB OH 20 MAY 85
FTD-ID(RS)T-1564-84

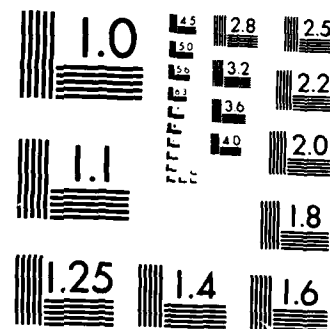
1/1

UNCLASSIFIED

F/G 20/5

NL





MICROCOPY RESOLUTION TEST CHART
NATIONAL BUREAU OF STANDARDS 1963 A

6/14
FTD-ID(RS)T-1564-84

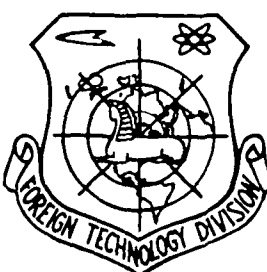
FOREIGN TECHNOLOGY DIVISION



APPLIED LASERS
(Selected Articles)

AD-A155 948

DTIC FILE COPY



2 DTIC
ELECTED
JUL 1 1985
A

Approved for public release;
distribution unlimited.



85 06 14 095

EDITED TRANSLATION

FTD-ID(RS)T-1564-84

20 May 1985

MICROFICHE NR: FTD-85-C-000348

Applied Lasers (Selected Articles)

English pages: 71

Source: Ying Yong Ji Guang, Vol. 3, Nr. 5-6, 1983
Vol. 4, Nr. 1, 1983, pp. 18-22; 25-27; 23-26;
27-30; 10; 31-34; 42; 35-37; 26; 38-42; 43-48;
36-37

Country of origin: China

Translated by: SCITRAN
F33657-84-D-0165

Requester: FTD/TQTD

Approved for public release; distribution unlimited.

THIS TRANSLATION IS A RENDITION OF THE ORIGINAL FOREIGN TEXT WITHOUT ANY ANALYTICAL OR EDITORIAL COMMENT. STATEMENTS OR THEORIES ADVOCATED OR IMPLIED ARE THOSE OF THE SOURCE AND DO NOT NECESSARILY REFLECT THE POSITION OR OPINION OF THE FOREIGN TECHNOLOGY DIVISION.

PREPARED BY:

TRANSLATION DIVISION
FOREIGN TECHNOLOGY DIVISION
WP-AFB, OHIO.

FTD -ID(RS)T-1564-84

Date 20 May 1985



Table of Contents

Graphics Disclaimer	ii
Single Mode High Power He-Ne Laser; by Wang Chunyao, Xin Zhenhua and Lin Tao	12
Modulation of Laser Beams by Magneto-Optic Garnet Single Crystal Films; by Liu Xianglin, Ruan Yuanji, Feng Jingzhang and Wang Hangxiang	16
Kinetic Studies of Ar ₂ F* in Fast Transverse Discharge Excited Ite-Ar-F ₂ Mixtures; by Gu Zhiyu, Wang Shaoying, D. Proch, F. Rebentrost, H. Webe and K.L. Kompa	24
Experimental Study on Mixing GDL with a Screen Nozzle; by Yu Gang, Zhao Jianrong, Fang Zhijia and Wu Chengkang	31
1 MeV REB Pumped Br ₂ * Molecular Laser and High Pressure XeBr Laser; by Wang Chanshan, Chen Yongrong, Xu Zhihai	40
CW Operated 1.55 μ m Proton-Bombarded Stripe InGaAsP/InP HD Laser at Room Temperature; by Wang Wei, Zhang Jingyuan, Tian Huiliang and Sun Furong	47
Investigation on Frequency Stability of Dye Lasers; by Yan Bingyu	56
Wavelength Demarcation of Tunable CO ₂ Laser by Wang Anning and Wu Nanzhan	69

GRAPHICS DISCLAIMER

All figures, graphics, tables, equations, etc. merged into this translation were extracted from the best quality copy available.

QUALITATIVE ANALYSIS OF FACTORS IMPROVING THE DISCHARGE STABILITY
OF HF CHEMICAL LASERS

Chen Yuming, Xu Jie, He Guozhen*

(Shanghai Institute of Optics and Fine Mechanics, Academia Sinica)

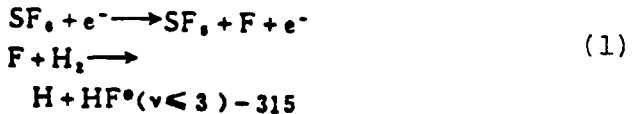
ABSTRACT

Several factors capable of improving the discharge stability of HF chemical lasers were investigated. Phenomena observed in experiments were qualitatively analyzed. Experimental results showed that the discharge characteristics had been improved with better results. /18**

The discharge characteristic of a HF chemical laser is very important to its performance. It directly affects the output power, light beam quality and equipment lifetime of the laser. Because SF₆ is a highly electronegative substance, it is extremely difficult to discharge stably and homogeneously in a gas mixture containing a high level of SF₆. We adopted several measures to obtain better results.

I. The Reaction Process

SF₆ was chosen as the fluorine donor, and H₂ was the hydrogen donor in this device. Major chemical reactions induced by the discharge are as follows:



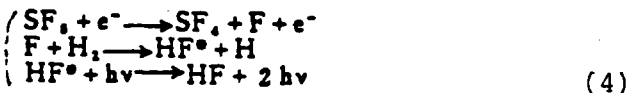
HF* may irradiate by either of the two reactions



* Received on January 24, 1983

** Numbers in margin indicate foreign pagination

Equation (2) is a spontaneous irradiation which can be neglected in reality. In addition, the reaction from SF_5 to SF_4 might also be present [1].



II. Structure of the Device

The cross section of the laser is shown in Figure 1. The discharge chamber was made of a transparent seamless plexiglass tube, 7.6 cm in inner diameter and 100 cm in length. A pair of electrodes were installed on the upper and lower walls of the tube. There are 16 terminal posts fastened to the holes behind the electrode. The effective length of the electrode is approximately 75 cm, and the gap is 2 cm. Ultraviolet preionization was used in the device. The preionization plates consisted of 30 stainless steel plates irregularly glued to a 84 cm long, 1.2 cm wide and 0.3 cm thick epoxy base plate. They were placed on either side of the device. An internal mirror type of resonance chamber was used. It was comprised of a 5 m radius gold-plated reflective mirror and a flat CaF_2 output coupling mirror. The mirrors were secured on the two end flanges. Their parallelism and concentricity could be adjusted by the six screws and three fine adjustment screws on the flanges. In order to effectively introduce electric energy to the SF_6/H_2 gas mixture, the fast Blumlein discharge circuit was used.

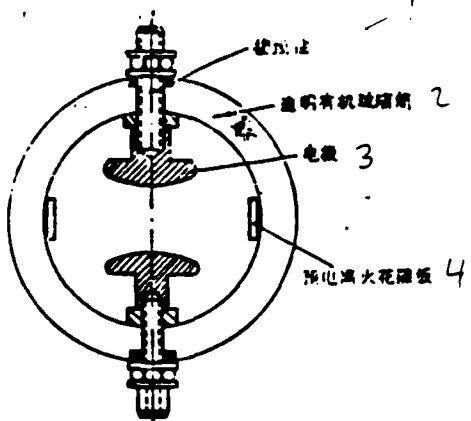


Figure 1.

1--Terminal post; 2-- Transparent plexiglass tube;
3--Electrode; 4--Preionization spark gap plate.

III. Measures

Gas Flow: In HF chemical lasers, serious corrosion occurs at the electrode surface due to the presence of ionized fluorine and the breakdown effect in the discharge process. Figure 2 clearly showed that there were apparent corrosion spots in seriously sparking areas as compared to other homogeneously discharging areas. This type of pollution increases due to the discharge reaction product built up near the electrode surface. It is particularly serious in a static condition. The electrical conductivity of this product can easily lead to serious sparking to aggravate the corrosion on the electrode surface. It not only reduces the energy output, but also shortens the lifetime of the laser. When the gas mixture is flowing, the situation is better. This is because the harmful product is removed from the discharge area before the next pulse arrives.

Selection of the Hydrogen Donor and Addition of He: It was experimentally discovered that the discharge could be strongly affected when the H_2 partial pressure exceeded 30 Torr. A lot of arc light began to appear. The homogeneity of the discharge could be greatly improved by the addition of a small amount of C_2H_6 to some hydrogen donors. This is because the ionization potential of C_2H_6 is smaller than that of H_2 (C_2H_6 : 12.8eV, H_2 = 15.6eV). The addition of a small amount of low ionization potential gas could improve the spatial homogeneity of the discharge [1]. On the other hand, C_2H_6 and C_2H_4 have larger photon ionization cross-sections than that of hydrogen $50 \times 10^{-18} \text{ cm}^2$, H_2 : $7 \times 10^{-18} \text{ cm}^2$).

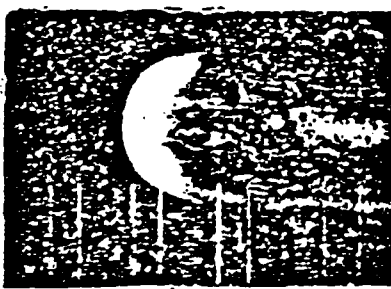
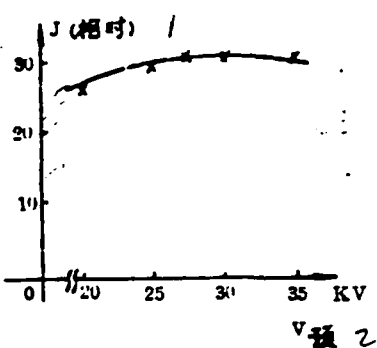


Figure 2

It is well known that inert gases could improve the uniformity of the discharge. When a laser is operating normally, the upper pressure limit without He is 180 Torr. With He, however, it could reach 250 Torr. The presence of He is necessary to avoid a breakdown. However, it was proven experimentally that the addition of He has no apparent effect on increasing the output energy; at least at low pressures.



($P_{\text{total}} = 120$ Torr, $P_{\text{SF}_6}/P_{\text{H}_2}^* = 7$, $V_{\text{primary}} = 30$ kV)

Figure 3.

($P_{\text{total}} = 120$ Torr; $P_{\text{SF}_6}^*/P_{\text{H}_2}^* = 7$, $V_{\text{primary}} = 30$ kV)
Key: 1--J(relative); 2-- $V_{\text{preionization}}$

Adaptation of preionization Technique: In order to improve the discharge uniformity in the electronegative SF_6 gas mixture, the ultraviolet preionization technique is effective. When $P_{\text{total}} = 120$ Torr, $P_{\text{SF}_6}/P_{\text{H}_2} = 7$ and $V_{\text{primary}} = 30$ kV, the energy output of the device was increased by approximately 10% when $V_{\text{preionization}} = 27.5$ kV as compared to the situation without preionization. Increasing preionization voltage could not significantly increase the energy output (Figure 3) because preionization itself could not enlarge the volume of discharge. It only could intensify the preionization spark to enhance the preionization effect. However, the purity of the gas will be reduced at excessively high voltages to shorten the lifetime of the laser.

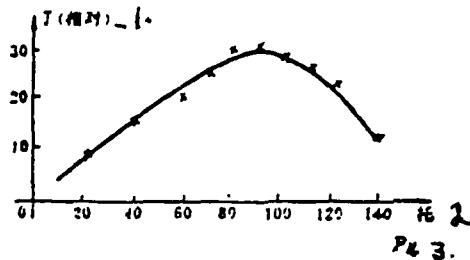
/20

Electrode Material: Experimental metallic electrodes could be made of brass, aluminum or stainless steel. From the corrosive effect of ionized fluorine and HF, it is least with stainless steel, followed by aluminum and brass. If the brass electrode surface is nickel plated, the corrosion could be significantly alleviated.

Because aluminum and brass electrodes are softer, the surface of the electrode might be polished to discharge more uniformly based on discharge tests. In terms of the life of the electrode material, an uncooled brass electrode has a short lifetime of 10^6 pulses. The lifetime of a stainless steel electrode is 10^9 pulses under the same condition. If it is water cooled, it can be lengthened by another order of magnitude. For a single pulse device, there is no problem with any electrode material. However, for a repetitive pulsing device such as a 100 Hz device, brass electrodes can only operate for 2.8 hours which is not tolerable.

In order to maintain the quality of discharge and reduce the formation of arc light, electrodes must be cleaned after a period of time of testing. The precipitate on the electrode surface might be removed with sandpaper and acetone.

Using Resistive Load Electrodes: Resistive load electrodes can suppress large discharge currents to consequently eliminate or reduce arc light. Graphite electrodes belong to this category. The energy output versus pressure curve for a device using this type of electrode is shown in Figure 4. The upper cutoff pressure is 140 Torr, and the lower one is 5 Torr. As compared to other metallic electrodes, the lower limit is very low. (The lower limit for metallic electrodes is around 20 Torr). It was experimentally found that the laser energy output using graphite electrodes at 90 Torr is equivalent to that with aluminum electrodes at 120 Torr. Furthermore, the uniformity of the discharge and the efficiency are superior to those of metallic electrodes. This indicates that resistive electrodes can produce a larger number of high energy electrons to ionize SF_6 than metal electrodes. It should have a bright future in eliminating arc light and producing a uniform glow discharge.



$(P_{SF_6}^*/P_{H_2}^* = 7, V_{primary} = 30 \text{ kV})$

Figure 4.

$(P_{SF_6}^*/P_{H_2}^* = 7, V_{primary} = 30 \text{ kV})$

Key: 1-- J(relative); 2--Torr; 3--P_{total}

Electrode Shape: It is very important to design an electrode with a uniform electric field across the surface because such electrodes are capable of producing a large volume of discharge in a transversely excited HF chemical laser to raise the ionization efficiency of SF₆ and to improve the conversion efficiency. They will directly influence the energy output and quality of the laser.

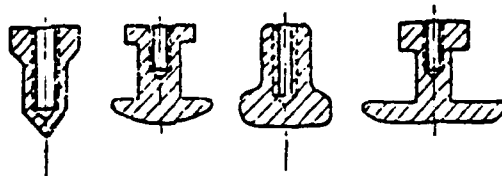


Figure 5

We designed four types of electrodes (see Figure 5). (I) is a pointed electrode and R1 is a small arc in the middle. It is easy to fabricate and discharges uniformly. However, the energy output is small because the discharge cross section is small.

TABLE 5. Comparison of Experimental Results with Four Types of Electrodes

1-电极面型	材料	4-区域宽2 (mm)	放电区域 4- (mm ²)	5-脉冲 4- (ns)	6-输出能盆 (J)	7-功率 (MW)	8-方向性 (mrad)	9-效率 (%)	10-能密度 (J/e)
(I)尖电极	黄铜 ¹²	0	16×6	90	0.477	5.185	6	1.683	6.80
(II)张氏电极 ¹³	黄铜 ¹⁴	5	20×8	90	0.698	8.019	6	2.462	4.05
(III)作图法电极	铝 ¹⁵	5	20×8	90	0.736	8.174	6	2.595	6.13
(IV)大平区电极	黄铜 ¹⁶	18	20×18	90	0.621	6.747	6	2.189	2.42

19. HF化学激光器运转条件: $P_{\text{总}} = 120 \text{ 托} P_{\text{SF}_6}/P_{\text{H}_2} = 4/1$, $V_{\text{主}} = 30 \text{ kV}$

Key: 1--Electrode surface shape; 2--material; 3--width of flat region; 4--discharge cross section; 5--pulse width; 6--output energy; 7--power; 8--directivity; 9--efficiency; 10--energy density; 11--(I) pointed electrode; 12--brass; (13)--(II) Chang's electrode; 14--brass; 15--(III) Schematic electrode; 16--Aluminum; 17--large flat electrode; 18--brass; 19--operating condition of HF laser: $P_{\text{total}} = 120 \text{ Torr}$, $P_{\text{SF}_6}/P_{\text{H}_2} = 4/1$, $V_{\text{primary}} = 30 \text{ kV}$.

(II) is the well known Chang's electrode [2]. The electric field between electrodes is very uniform. Its smoothness and closeness are also superior to other types of electrodes. The gap is a key parameter for this type of electrode. The shape varies with the gap. (III) was designed schematically from experience. The flat area in the middle is smoothed out from two radii of curvature R. It is easy to design and fabricate. Experimental results showed that the results were very good. (IV) is a large flat electrode. The width of the flat area of the electrode is expanded to increase the discharge volume. However, this causes a great deal of difficulty in the uniformity of the discharge. From Table 1, one can see that the schematic electrode and Chang's electrode are better than the pointed electrode and the large flat electrode. Although it is easy to discharge through pointed electrodes, yet the discharge cross section is very small and the energy output is very low. The discharge cross section of the large flat electrode is the highest. But, the uniformity of the discharge is poor. There are more arcs and the energy density is very low. It should also be pointed out that the

directivity and pulse width of the laser beam are not related to the choice of electrode. The former is determined by the cavity shape, while the latter is determined by pressure because pressure is the primary factor affecting the relaxation rate.

IV. Experimental Results and Analysis

Using the schematic aluminum electrode as an example, the dependence of the laser energy output on the composition of the gas mixture is shown in Figure 6. The maximum r value is 5. The fact that the energy output decreases at a nonoptimal r value may be attributed to the reason that the amount of HF produced through the fast reaction (1) by H_2 is insufficient at high r values. When the total pressure remains unchanged, any increase in the SF_6 concentration corresponds to a decrease in the H_2 concentration. The decomposed F atoms cannot react completely with H_2 based on Reaction (1). The input energy is consumed excessively in the ionization of unnecessary SF_6 which leads to a decrease in the energy output. At low r values, however, the F atom concentration decreases with decreasing decomposition of SF_6 . This leads to an excess of H_2 molecules to complete Reaction (1). In this case, not only more H_2 molecules are ionized to consume more input energy, but also H_2 is a good deactivating agent to lower the energy output. Excess H_2 molecules can deactivate HF (v) via collision $HF(v) + H_2 \rightarrow HF(v-1) + H_2$. The maximum energy is attained when the maximum amount of pure HF is produced in the laser pulsing period.

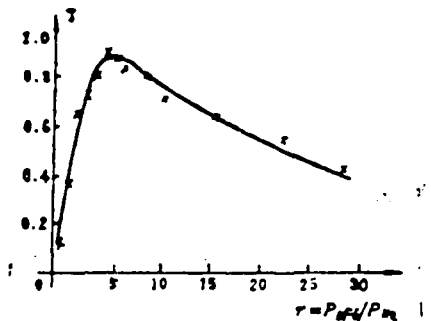


Figure 6. ($P_{\text{total}} = 120$ Torr, $V_{\text{primary}} = 32$ kV,
 $V_{\text{preionization}} = 27$ kV)

Key: 1 -- $r = P_{SF_6}/P_{H_2}$

In order to avoid the "locking" area, the laser top should operate in the $|\Delta f| > |\Delta f_b|$ region. The single crystal garnet film magneto-optic phase modulator could be used as a bias element. This type of device creates a phase shift, $\Delta\phi$, between two light beams propagating in opposite directions based on the transverse Kerr magneto-optic effect to achieve the frequency biasing effect, i.e.,

$$\Delta f_b = \frac{(\Delta\phi/2\pi)c}{L} \quad (9)$$

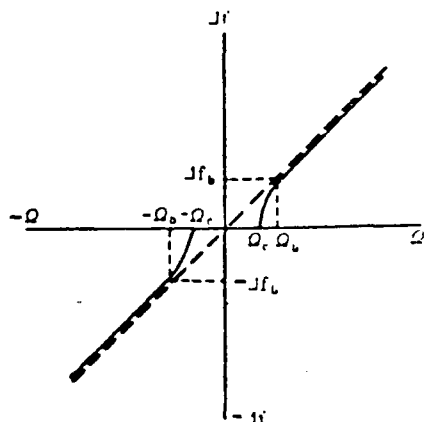


Figure 7. Pitch frequency Δf vs. angular speed Ω

A single crystal $(\text{BiPrGdYb})_3(\text{TeAl})_5\text{O}_{12}$ thin film was prepared as a magneto-optic phase modulator as a magnetic mirror frequency biasing element. It was used in a 60 cm long, $1.15 \mu\text{m}$ wavelength laser top. Its optical path is shown in Figure 8. When an external dc field is present, the measured beat frequency of the laser top is $> 10 \text{ KHz}$. When the external field is alternating at 50 Hz, an alternating beat frequency was observed (see Figure 9). The alternating magnetic field is 0 twice in each cycle (0.02 sec), which corresponds to the locking area of the beat frequency. Using the magneto-optic modulator as a magnetic lens frequency biasing device enables the top to stay away from the locking area. It can operate in the linear region on the Δf - Ω curve under the frequency biasing effect. Consequently, the principle of a magnetic lens frequency biasing top was tested.

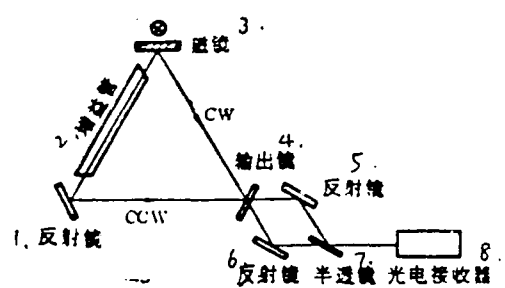


Figure 8. Schematic diagram of the optical path of the laser top. 1--reflective mirror; 2--gain tube; 3--magnetic lens; 4--output mirror; 5--reflective mirror; 6--reflective mirror; 7--semi-transparent mirror; 8--opto-electric receiver

magnetizing coil, the reversal of the magnetic strength in a magneto-optic medium is realized by the displacement of the domain wall. The displacement of the domain wall, however, is slow. There is loss due to magnetic hysteresis. Therefore, this type of magneto-optic modulation has a frequency upper limit [4]. In our experiment, the magneto-optic modulator described above could operate in the 6 Hz-30 KHz range. At 1 KHz, the modulating power is 20-200 mW.

The aforementioned magneto-optic modulator has already been used in a Faraday rotation detector. The accuracy is $\pm 0.05^\circ$. It can be used to measure the θ_F , T_C and magnetic hysteresis curve of a material [5]. It is also used in the model WZZ-1 polarimeter. As compared to the original ZF₆ glass modulator, the modulating field is lower (<100 Oe), the volume is smaller ($\leq 25 \times 30 \text{ mm}^3$), and the weight is less (<100g). Furthermore, there is little thermal effect. The requirements of low power consumption, measurement accuracy and stability can be all met.

Magneto-optic phase modulation

In a laser top, two light beams traveling in opposite directions can be used to detect the rotation of an object. Two light beams propagating toward opposite directions can resonate at slightly different frequencies. This frequency difference is

$$\Delta f = \frac{4A\Omega}{L\lambda} \quad (7)$$

where A is the area enclosed by the laser loop, L is the optical path of the laser loop, Ω is the component of the rotation rate of the object in the normal direction of the ring surface, and λ is the laser wavelength. However, when Ω is small, they can be locked at the same frequency because of the weak back scattering coupling of two light beams. Hence, the measured $\Delta f-\Omega$ curve (see Figure 7) can be expressed as:

$$\Delta f = \begin{cases} 0 & \text{when } \Omega < \Omega_c \\ \frac{4A}{L\lambda} \sqrt{\Omega^2 - \Omega_c^2} & \text{when } \Omega > \Omega_c \end{cases} \quad (8)$$

meters through the magneto-optic modulator, the contents of the broadcast could be clearly heard through the speaker; when the modulating frequency is 1 KHz, the modulation pattern is shown in Figure 3. If it was modulated by the 50 Hz and 1KHz magneto-optic modulators separately, then the pattern obtained is as the one shown in Figure 4.

If $\beta = 45^\circ$, then the modulation depth can be derived from equation (5)

$$m = \sin 2\phi_F \quad (6)$$

Figure 5 shows the maximum magneto-optical modulation depth and the light absorbance of a $h = 8.43 \mu\text{m}$ modulator. The maximum modulator depth is determined by the θ value of the material. Furthermore, it is a function of wavelength. The thicker the magneto-optic medium is (the same material), the larger the modulation depth becomes. Light absorbance also varies significantly with wavelength. The longer the wavelength is, then the smaller the absorbance becomes. In the near infrared region ($\lambda > 1.1 \mu\text{m}$) $\alpha < 2 \text{ cm}^{-1}$.

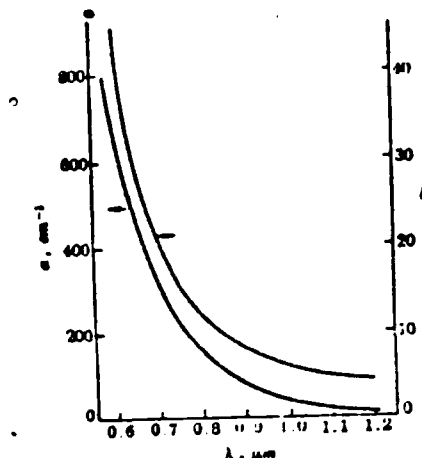


Figure 5. Characteristic curve of the magneto-optic modulator

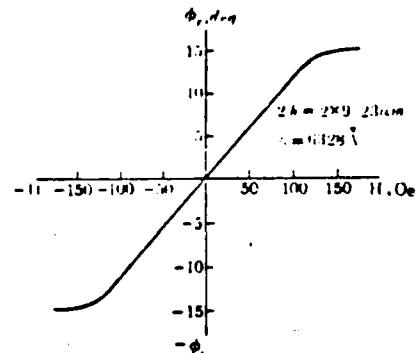


Figure 6. Relation between Faraday rotation ϕ_F and external magnetic field H

Figure 6 shows the relation between the static ϕ_F and the external magnetic field H as measured on an X-Y recorder. When a variable current at a certain frequency is sent into the

From equations (3) and (5), one can see that I_m only varies with H . H , however, is proportional to the magnetization coil current i . Consequently, I_m can be modulated by i .

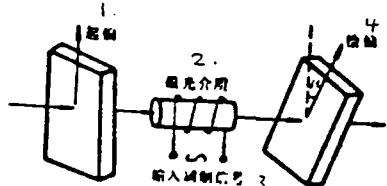


Figure 1. Schematic diagram of a low frequency magneto-optic modulator
1--polarizer; 2--magneto-optic medium; 3--input modulating signal; 4--analyzer

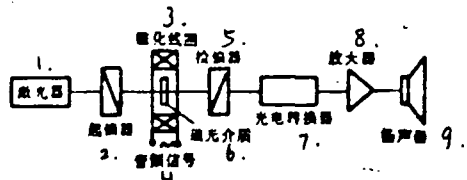


Figure 2. Optical path of broadcasting
1--laser; 2--polarizer; 3--magnetization coil; 4--sound frequency signal; 5--analyzer; 6--magneto-optic medium; 7--opto-electric converter; 8--amplifier; 9--speaker

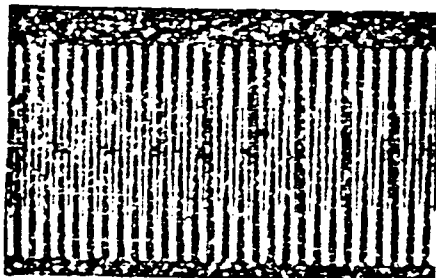


Figure 3. 1kHz modulated optical signal

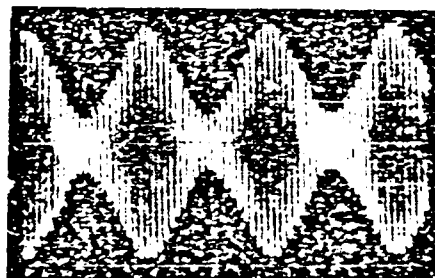


Figure 4. Optical signal doubly modulated at 1kHz and 50 Hz

Single crystal $(\text{BiTm})_3(\text{FeGa})_{50}^{12}$ film was used as a magneto-optic medium in fabricating a 15mm diameter aperture modulator whose external dimensions (including magnetizing coil and polarizers) are 25 cm in diameter and 30mm in length. It was used in an optical path such as the one shown in Figure 2. The output power of the laser was 2 mW and the wavelength is 6328 Å. A photomultiplier or silicon solar cell detector was used. If the sound signal of a semi-conductor radio was used as the modulating signal at the input of the magnetizing coil and the optical information was allowed to be transmitted for over 20

magneto-optic ratios are 2.90 and 4.05 deg/dB, respectively. The major characteristics are shown in Table 1.

Magneto-optic modulation of light intensity

The light intensity can be modulated based on the principle that the polarization plane might be rotated when a polarized light travels through a magnetized magnetic medium. The structure of a low frequency magneto-optic modulator is shown in Figure 1. The magneto-optic material was placed in a magnetization coil and the coil was located between the polarizer and the analyzer.

If the anisotropy of the crystal is neglected, then the saturated magnetic field required to magnetize the specimen is

$$H_s = N4\pi M_s \quad (1)$$

where N is the demagnetization factor which is determined by the sample shape and magnetization direction. Its numerical value is between 0-1. If the magneto-optic effect of the substrate is neglected, then the Faraday rotation of magnetic saturation is

$$\phi_s = \theta_F 2h \cos \gamma \quad (2)$$

where γ is the angle between the direction of magnetization and the direction of light propagation, h is the thickness of a single-sided film and $2h$ is a double-sided film. For unsaturated specimens, the Faraday rotation is

$$\phi_F = \frac{H}{N4\pi M_s} \theta_F 2h \cos \gamma \quad (3)$$

where H is the external magnetic field. If the loss in the polarizer can be neglected, then according to Malus law, at the analyzer the light intensity of a light beam whose initial intensity is I_0 at the polarizer is

$$I = I_0 \cos^2 \beta \quad (4)$$

β is the angle between the polarization axis of polarizer and that of the analyzer. If a magneto-optic modulator is added between the two polarizers, then the light intensity passing through the analyzer is

$$I_a = I_0 e^{-\alpha n} \cos^2(\beta + \phi_F) \quad (5)$$

by neglecting the substrate loss and the reflection and interference of the magneto-optic medium.

Since LeGraw reported a magneto-optic garnet modulator in 1966, Domanski [1] studied it further in 1981. However, it was limited to using single crystal $Y_3Fe_5O_{12}$ in bulk at $\lambda \geq 1.15\mu\text{m}$. Tien, et al., [2] reported the modulation of light with a single crystal garnet film. We used a Bi containing single crystal garnet film as a magneto-optic medium to fabricate a light intensity modulator operating in the visible region (6328 Å) [3]. In this paper, the modulation of laser light intensity at 6328 Å with a magneto-optic $(\text{BiTm})_3(\text{FeGa})_5O_{12}$ single crystal film and the magneto-optic phase modulation at 1.15 μm with single crystal $(\text{BiPrGdYb})_3(\text{FeAl})_5O_{12}$ film were reported.

TABLE 1. Performance characteristics of two magneto-optic single crystal garnet films

1. 性 种 类 能	3. 膜厚 h (μm)	4. πM_s (Gs)	居里温度 T_c (°C)	易磁化 方 向	λ = 6328 Å			
					6. 折射率 n	7. θ_F (deg/cm)	8. α (cm ⁻¹)	9. θ_F/α (deg/dB)
$(\text{BiTm})_3(\text{FeGa})_5O_{12}$	7.38	150	145	7. 垂直膜面	2.30	8130	649	2.90
$(\text{BiPrGdYb})_3(\text{FeAl})_5O_{12}$	5.06	200	185	8. 平行膜面	2.34	9320	529	4.05

1--type; 2--characteristics; 3--film thickness h (μm); 4--Curie temperature T_c (°C); 5--magnetization direction; 6--index of refraction n; 7--perpendicular to the film; 8--parallel to the film

Magneto-optic single crystal garnet films

The Bi-doped magneto-optic single crystal garnet film is a new class of optical information material. It has a high Faraday rotation ratio Q_F , an appropriate light absorbance α , a large magneto-optic ratio Q_F/α and an adjustable saturated magnetization. Therefore, it can be used in magneto-optic modulators, magneto-optic insulators, laser tops, high voltage current detectors, magneto-optic storage devices, magneto-optic wave guides, graphic displays, magneto-optic deflectors and magneto-optic bubble devices. We used an isothermal liquid phase epitaxy method to grow $(\text{BiTm})_3(\text{FeGa})_5O_{12}$ and $(\text{BiPrGdYb})_3(\text{FeAl})_5O_{12}$ magneto-optic single crystal films on a (111) $\text{Gd}_3\text{Ga}_5O_{12}$ substrate. The

of different diameters as the discharge tube. The radial end of the capillary was used as the output end. In this case, whether the output end is spherical or flat has little effect on the diameter of the light beam, especially in a long cavity with a large radius of curvature.

The coherent length can be measured by the simple Michelson interferometry. Because of the single mode output, the coherent length has to be long. Because we are limited in our laboratory, it does not make any sense to perform this experiment when we can only measure a light path difference of a few meters. This laser was used to photograph a 1 m^2 machine tool. It only took 3 seconds for exposure. The hologram was clear, which is evidence supporting that the coherent length was extended (see Figure 3). Usually holographic photography does not require an excessively long coherent length. If a 37 mm thick etalon is used, the laser beam includes three longitudinal modes. Its coherent length is more than 2 meters, which is adequate in practical applications.

References

- (1) L.G. Deshayer, *Appl. Opt.*, 6, 431 (1967).
- (2) M. Hercher, *Appl. Opt.*, 8, 1103 (1969)

/27

Modulation of laser beams by magneto-optic garnet single crystal films

/23

Liu Xianglin, Ruan Yuanji, Feng Jingzhang and Wang Hangxiang
(Shanghai Institute of Metallurgy, Academia Sinica)

ABSTRACT

Experimental results of laser light intensity modulation at 6328 \AA with single crystal magneto-optic $(\text{BiTm})_3(\text{FeGa})_5\text{O}_{12}$ film modulator and magneto-optic phase modulation at $1.15\text{ }\mu\text{m}$ with single crystal $(\text{BiPrGdYb})_3(\text{FeAl})_5\text{O}_{12}$ film magnetic mirror bias device were reported.

mode output can only be obtained at a specific position. After the laser began to lase, mode jumping occurred every dozens of seconds initially. Then, it gradually lengthened. After nearly 1 hour of warmup, the mode jumping time was extended to above 5 minutes. Initially, the mode jumped sequentially until it was completely shifted outside the envelope of the gain curve and the power approached zero. After warming up for a considerable period of time, mode jumping might still occur. However, it did not move in one direction as before. This was caused by thermal instability. Because the mode jumping time is much longer than the holographic exposure time, this device is suitable for holographic applications. It is simple and economic and does not need any additional feedback servo-system for stabilization.

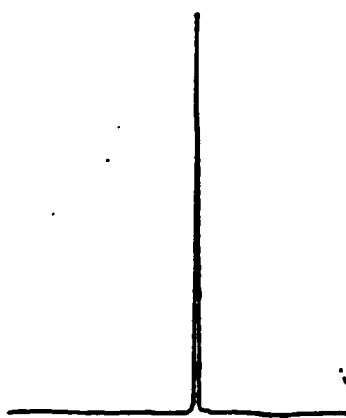


Figure 2. The Single Mode Obtained with a 51.3 mm Thick Etalon.



Figure 3. A Hologram Taken with a Single Mode Laser.

Reference [2] reported that the loss could be minimized by placing the etalon at the end where the light beam diameter was larger and used it as the output lens. It is usually a spherical end. In this case, the maximum single mode power output can be obtained. However, we did not observe this phenomenon in our experiment. This might be because we used two connected capillaries

TABLE 2. Laser Power Output and Longitudinal Modes after Inserting Etalons with Various Reflectivity.

1. 表面反射率%	2. 输出功率mW	3. 纵模数
4	39	18
13	22	14
17	21	13
26	14	11
34	3	6

4-3 表中均为10毫米厚的玻璃标准具

Key: 1--Surface reflectivity; 2--Power output; 3--Longitudinal mode number.; 4-- A10 mm thick glass etalon was used for all cases in the table.

refraction. The reflectivity of the surface is somewhat directly related to its fineness. It is possible to reduce multi-mode resonance by increasing the fineness. In this case, the etalon loss is primarily due to transmission loss at the surface. It was demonstrated experimentally that the laser beam could be totally consumed by the insertion of a etalon into a low gain He-Ne laser. Therefore, it is not advisable to obtain a single mode resonance by using a thin etalon with a surface reflective coating. This mode selection is created by the coherence among all the lenses in Figure 1. It is different from the mode selection with an uncoated etalon as described above.

Figure 2 shows the single longitudinal mode laser line after a 51.3 mm quartz etalon was inserted in the cavity. Almost all the power is concentrated in the single line. The gain curve appeared to be broadened uniformly.

When the etalon is perpendicular to the optical axis, the maximum power output cannot be obtained. In this case, two modes may appear simultaneously. Therefore, the etalon must be tilted slightly with respect to the optical axis. The maximum single

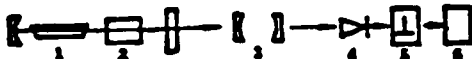


Figure 1. Experimental Apparatus of the Selective Mode Laser.

We used quartz and glass etalons with various thicknesses and surface reflectivity to study the effect on the power output and the mode. Table 1 shows the experimental results in terms of etalon thickness versus power and longitudinal mode number. One can see that a 64 mW single mode output was obtained from a 80 mW multiple mode laser when a quartz etalon was used. The power loss is only 20%. If a glass etalon is used, the loss is 80%. The single pass gain of the He-Ne laser is low. It falls on the transmission peak of the F-P loss peak. This is primarily attributed to scattering. Therefore, it is necessary to choose quartz as the etalon material because its scattering loss is low. In addition, when the parallelism of the etalon is increased from 1" to 2", the output power will be reduced by another 13%.

TABLE 1. Laser Power Output and Longitudinal Modes after Inserting Etalons of Various Thickness

/26

1. 标准具厚度mm	材料	输出功率mW	纵模数
5. 无		80	23
51.3	6石英	64	1
49.5	7玻璃	15	1
37.0	8玻璃	16	3
24.0	9玻璃	18	11
10.0	10玻璃	39	18

Key: 1--Etalon thickness mm; 2--material; 3--power output mW; 4--longitudinal mode number; 5-- none; 6--quartz; 7--glass; 8--glass; 9--glass; 10--glass.

Table 2 shows the power output and longitudinal modes obtained with the glass etalons of the same thickness (10 mm). The surface was coated with a thin film of different index of

SINGLE MODE HIGH POWER He-Ne LASER

/25

Wang Chunyao, Xin Zhenhua and Lin Tao

(Shanghai Institute of Laser Technology)

ABSTRACT

A single longitudinal mode He-Ne was developed by using a tilted etalon inside the resonator, resulting in 64 mW of single mode power output from a 80 mW Model 2000 A laser.

As a He-Ne laser for holographic applications, it is desirable to have a high power output and long coherent length. However, these two requirements are contradictory. Due to the interference of axial modes in the laser beam, the effective coherent length of a high power commercial laser is very short. It is less than 20 cm for a 2 m long cavity laser. In the past, there were many attempts to reduce or limit the modes [1]. Although they are effective in reducing multi-mode operation, however, the power output is very low. To insert an F-P etalon into the cavity is a simple and effective method to limit multiple modes and to lengthen the coherent length [2]. The relation between its periodic bandpass and the gain of the laser medium only allows one or several resonance modes with reasonably high power output.

This experiment was performed using a Model 2000 A laser as shown in Figure 1. In order to install a fine angular adjustment device for the etalon, the discharge tube was shortened by 20 cm. The actual discharge length is 1.8 m. The laser beam, after passing through a scanning interferometer at better than 250 in fine constant, was absorbed by a photodiode. The signal was amplified and transmitted to a Model PM 3310 oscilloscope and plotted by a Model 601 X-Y recorder. The laser power was measured by a Model JK-1 power meter.

be maintained at more than 90% of the initial value.

REFERENCES

- [1] R. Paulson, J. Appl. Phys. 44, 5633 (1973).
- [2] T.T. Chang, Rev. Sci. Instru. 44, 405 (1973).

Figure 8 shows the dependence of energy output on the main discharge voltage. One can see that the laser energy is linear with respect to the input voltage. At a fixed pressure, an increase in discharge voltage can in fact proportionally increase the number of high energy electrons to dissociate SF₆. Furthermore, it was also experimentally proven that the increase in the energy output with the input voltage is more gradual at a lower pressure (such as 60 Torr) as compared to a higher pressure (such as 120 Torr). This relative insensitivity at low total pressures is because the number of high energy electrons capable of dissociating SF₆ increases for less at low pressures as compared to that at high pressures with increasing input voltage. Again, it was proven that the laser output depends on the number of SF₆ molecules to be dissociated into F atoms and the number of electrons with sufficiently high ionization energies. However, the discharge voltage cannot be raised unlimitedly. Otherwise, it may lead to a capacitive breakdown.

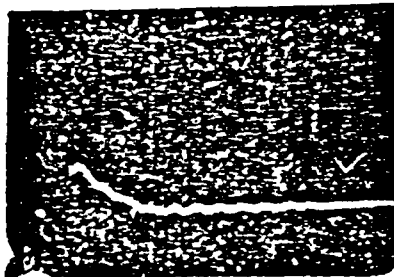


Figure 9.

The discharge characteristics of HF chemical lasers have an important effect on the energy output, quality and stability of the device. Figure 9 shows the superposition of 5 laser waveforms. This indicates that the laser beam is relatively uniform. The stability and reproducibility of the device have reached a certain standard. When the total pressure is 120 Torr, $r = 7$ and primary discharge voltage is 34 kV, the maximum energy of the pulse can reach above 1 joule. The efficiency is 3.2%. The device can operate once every 2 minutes under static conditions. The energy of the 100th pulse can

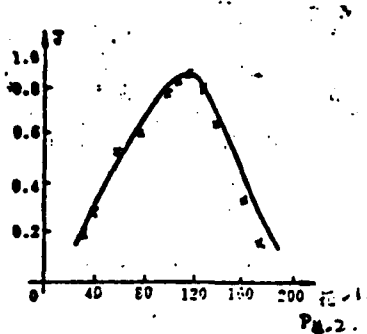


Figure 7. ($V_{\text{primary}} = 32 \text{ kV}$, $V_{\text{preionization}} = 27 \text{ kV}$, $r=5$).

Key: 1--Torr; 2- P_{total}

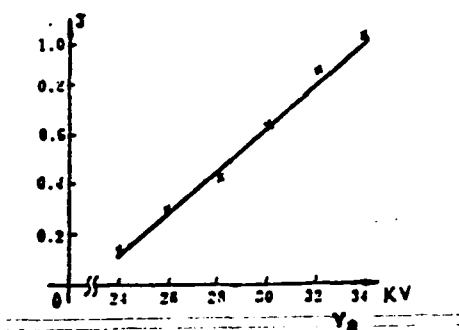


Figure 8. ($P_{\text{total}} = 120 \text{ Torr}$, $V_{\text{preionization}} = 27 \text{ kV}$, $r = 5$)

At the optimal composition ratio $r = 5$, the relation between the laser energy output and the total pressure is shown in Figure 7. Corresponding to a primary discharge voltage, there is an optimal total pressure. For aluminum electrodes, V/P was estimated to be 270 V/Torr. Therefore, at the optimal ratio ($r=5$) and a fixed voltage (37.5 kV) the laser energy increases with increasing pressure to finally reach saturation. Because there are not enough SF_6 molecules to be dissociated and not enough electrons with sufficient energy to dissociate SF_6 , the gas density (although very low) has some effect on the collision probability at the optimal total pressure of 120 Torr. Since the free path of electrons is long, there are more electrons with high ionization energies. Conversely, the output energy decreases with increasing pressure at one optimum pressure. This is because the molecular density is increased at high pressures. The probability of collision increases and the free path of electron is reduced. When the main discharge voltage remains unchanged, the number of high energy electrons capable of dissociating SF_6 is decreased, leading to the further decrease of the energy output. /2

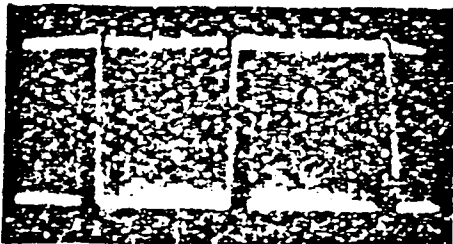


Figure 9. Beat frequency signal under alternating magnetic field

Acknowledgement: The authors wish to acknowledge the results on the laser top experiment provided by Qinghua University and the application report of the model WZZ-1 polarimeter given by the Shanghai Optical Instrument Repair Plant.

References:

- [1] A. Domanski and R. Maslanka, *Appl. Opt.*, 20 (24), 4245 (1981).
- [2] P. K. Tien et al, *Appl. Phys. Lett.*, 21 (8), 394 (1972).
- [3] 上海冶金所磁光组, *激光*, 7(9), 63 (1980).
- [4] R. W. Coopr and T. L. Page, *Radio and Elect. Eng.*, 39 (6), 302 (1970).
- [5] 袁元绩等, *《仪器仪表学报》*, 4, (4), 339 (1983).
- [3] Magneto-optic Group in Shanghai Institute of Metallurgy, *Laser*, 7(9), 63 (1980).
- [5] Ruan Yuanji et al, < *Journal of Instruments and Panels* >, 4, (4), 339 (1983).

/26

Gu Zhiyu and Wang Shaoying
(Anhui Institute of Optics and Fine Mechanics, Academia Sinica)

D. Proch, F. Rebentrost, H. Webe and K. L. Kompa
(Max-Planck Institut fuer Quantenoptik, D-8046 Garching,
Fed. Rep. Germany)

ABSTRACT

Various fluorescence observations on ArF^* and Ar_2F^* were made through the fast transverse discharge excited He-Ar-F₂ gas mixture. Time-resolved and time-integrated spectra were obtained. The spontaneous radiation lifetime of Ar_2F^* and the quenching rate constant of F₂ with respect to Ar_2F^* were measured. Finally, the formation kinetics of Ar_2F^* by electric discharge was suggested and analyzed.

Velazco and Selser first observed the radiation of excited rare gas-halogen quasi-molecules from the strongly bound excited state to the repulsive ground state. Soon afterward, they reported the detail spectra, structure analysis and potential curve calculation. In investigating this type of diatomic quasi-molecules, a new type of rare gas-halogen excited quasi-molecules, the triatomic molecules, was discovered. The continuous radiation band of this triatomic quasi-molecule is considered to be transition between the ionically bound excited state to the covalently repulsive state. In the latter case, it dissociates into ground state atoms.

The triatomic quasi-molecule Ar_2F^* has a continuously radiating band centered at around 290 nm. Hence, it may be developed into a tunable ultraviolet laser. The kinetics of Ar_2F^* in gas mixtures of Ar-F₂ and Ar-NF₃ was studied by Nakano Lorents, Marowsky, et al., using electron excitation, and by Chen using proton excitation. To date, there is no corresponding data obtained directly by electric discharge.

There are two areas worthwhile for our attention in discharge excitation. (1) Low energy electrons have a larger excitation cross-section. The pumping efficiency is high. (2) The pulse repetition rate is high which makes high mean laser power possible. It is very important to the feasibility of a direct charge pumped Ar_2F^* laser that the kinetics of the discharge process is understood.

Our work on kinetics of the $\text{He}|\text{Ar}|\text{F}_2$ mixture in TEA discharge is reported in this paper. The partial pressures of these three gases were varied. Because the electron temperature is lower /28 at discharge as compared to electron beam excitation, a different reaction kinetics was expected. On the basis of experimental observations, various routes for Ar_2F^* formation were suggested. In addition, the radiation lifetime of this compound and its F_2 quenching rate constant were also reported.

Experimental apparatus

The experimental apparatus is shown in Figure 1. The TEA fast discharge device was referred in a separate paper. The primary capacitor (200 nF) was charged to 36 kV. It charged a series of 40 nF pre-ionization capacitors by resonance to produce the fast discharge. The pumping power density was estimated to be 30 MW/cm^3 . The gas mixture was premixed in the circulating system before entering the discharge chamber. Partial pressures and total pressure were measured by pressure gauges.

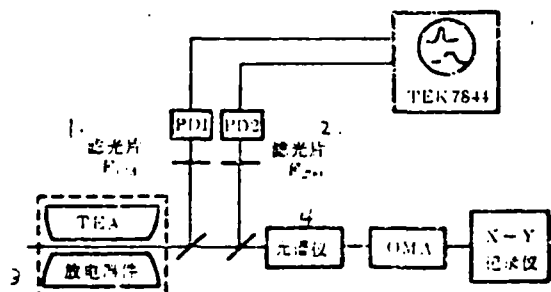


Figure 1. Experimental apparatus.
 1--filter--2--filter;
 3--discharge device; 4--spectrophotometer

The ranges of pressure are:
 F_2 : 0.05-6 mPa, He: 50-3800 mPa
 and Ar: 50-2500 mPa. The partial pressure ratio, He to Ar, ranged from 60: 1 to 1:2. The total pressure was ≤ 1000 mPa.

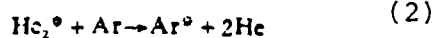
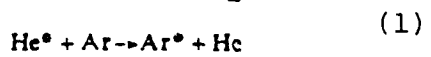
An ultraviolet sensitive OMA system (B+M Spektronik,

model OSA500 with scintillators) was connected to a spectrophotometer to record the time-integrated spectra. The time-resolved spectra for ArF^* and Ar_2F^* were measured with a fast photodiode (Hamamatsu R617 S-5) connected to a dual beam oscilloscope. Thus, two filters could separate ArF^* (193 nm) from Ar_2F^* (290 nm).

Formation of Ar_2F^*

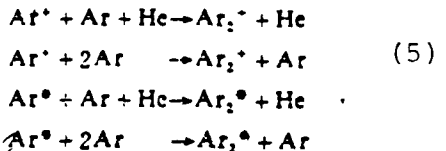
Before giving the results of this work, it seems to be necessary to list all the major possible processes to form excited materials in the $\text{He}|\text{Ar}|F_2$ mixture to build up a basis for explaining these results.

Excited or ionized Ar atoms are created by direct electron collision or through collision with He^* or He_2^* :

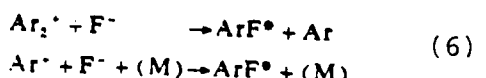


As compared to (2), (3) and (4), reaction (1) is a slow process.

Through the following ternary reactions, excited and ionized Ar atoms can form dimers:



The formation of ArF^* is considered to be an ion-ion recombination (M is any collision subject):



Or, it can be formed through the following reaction:



Finally, these excited or ionized dimers are participating in the following reactions to form the triatomic quasi-molecule Ar_2F^*

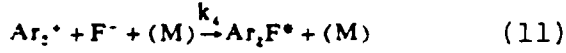
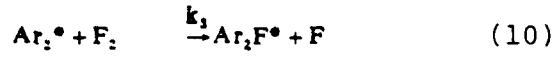
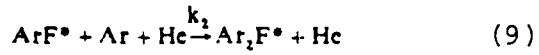
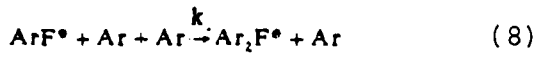


Figure 2 intuitively expresses the formation mechanisms of ArF^* and Ar_2F^* through reactions (5)-(8).

The rate equation for the kinetic formation of Ar_2F^* is

$$\frac{d}{dt}[\text{Ar}_2\text{F}^*] = k_1[\text{ArF}^*][\text{Ar}]^2 + k_2[\text{ArF}^*] \\ [\text{Ar}][\text{He}] + k_3[\text{Ar}_2^*][\text{F}_2] \\ + k_4[\text{F}^-][\text{Ar}_2^*][\text{M}] \quad (12) \\ - \frac{[\text{Ar}_2\text{F}^*]}{\tau}$$

τ is the effective attenuation coefficient of Ar_2F^*

$$\tau^{-1} = \tau_{290}^{-1} + k_5[\text{F}_2] + k_6[\text{Ar}] + k_7[\text{He}] \\ + k_8[\text{Ar}]^2 + k_9[\text{He}]^2 + k_{10}[\text{Ar}][\text{He}] \quad (13)$$

τ_{290} is the radiation lifetime of Ar_2F^* and k_i is the quenching rate constant of Ar_2F^* by the particle in the parenthesis.

Results and analysis

From the fluorescence time resolution measurements of ArF^* and Ar_2F^* , one can see that (from Figure 3):

(1) After the ArF^* radiation peaked and declined to a smaller value, the Ar_2F^* radiation rose to its maximum. This supports the concept that ArF^* is the precursor of Ar_2F^* which is in agreement with the viewpoint of Marowsky, et al.

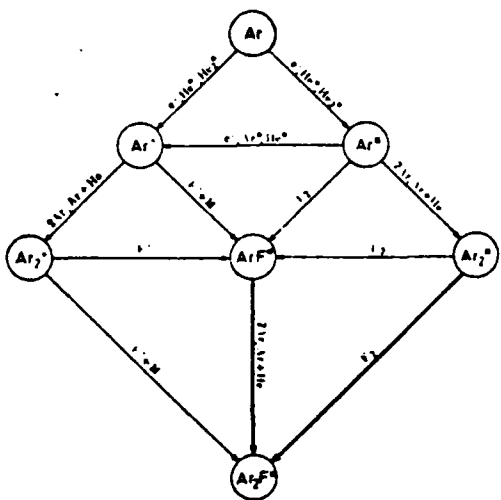


Figure 2. Formation mechanisms of ArF^* and Ar_2F^* in electrically discharged gas mixture of He-Ar-F_2

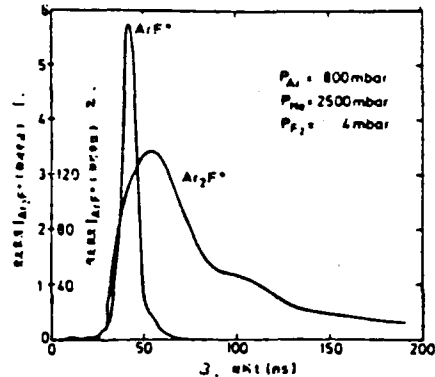


Figure 3. Time-resolved spectra of ArF^* and Ar_2F^*
 1--fluorescence intensity $|\text{Ar}_2\text{F}^*$ relative scale);
 2--fluorescence intensity $|\text{ArF}^*$ (relative scale); 3--time t (ns)

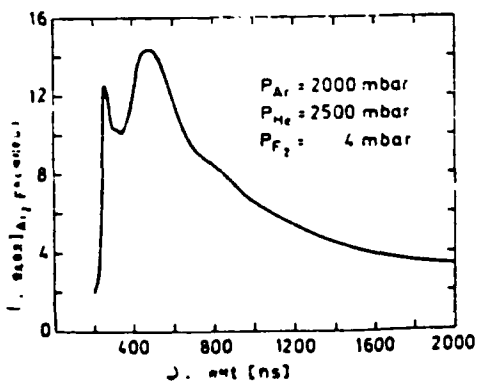


Figure 4. Time-resolved signal measured with varying gas parameters: growth of second Ar_2F^* component is the major component of the entire waveform.
 1--fluorescence intensity $|\text{Ar}_2\text{F}^*$ relative scale); 2--time t (ns)

l--fluorescence intensity $|\text{Ar}_2\text{F}^*$ process is related to Ar_2F^* . The slow process must be slower than the radiation lifetime of Ar_2F^* . Otherwise, the second peak would not be separated. There must be a slow energy transfer process and ion-ion recombination.

(2) The Ar_2F^* waveform is the superposition of two processes whose peaks appeared at different times. Its attenuation is also not a simple exponential decay process. One can deduce that this triatomic quasi-molecule has more than one precursor. The fast and slow decay rates reflect two formation mechanisms of different time scale. From the waveform, one knows that the fast formation process is related to Ar_2F^* . The slow process must be slower than the radiation

If the Ar pressure rises from 800 mPa (Figure 3) to 2000 mPa (Figure 4), its contribution to the formation process may vary

significantly. The second component of Ar_2F^* radiation began to appear at 800 mPa of Ar pressure. It grew and became the major portion of the entire waveform. In the meantime, the second peak was further lagging behind the first peak. From Figure 4, /29 the exponential decay coefficient of the second peak is 500 ns.

In the two above figures, the effect of the pressure on the fluorescent signal is secondary. This is because such changes are not important for reactions (1)-(4).

Increasing the density of Ar atoms favors the binary reaction (5). In view of the fact that the electron temperature is lower, ionic reactions are not important. Increasing Ar_2^* , however, can significantly increase the contribution of reaction (10). Based on the above reason, the effect of reaction (11) is not important. Compared to the data obtained by electron excitation (transverse and longitudinal), the second peak did not appear in the fluorescence intensity measurement. Because of the high electron energy, ionic reactions (5) and (6) are primary. The formation of Ar_2F^* will take the ArF^* route (equations (8) and (9)).

A second peak was observed by coaxial electron excitation at higher Ar pressures than those used in this experiment because electrons were entering an oscillating potential field in the tubular anode filled with the lasing gas. The electron energy was rapidly lost through multiple collisions. Consequently, the coaxial electron temperature is much lower than that in the transverse direction. This explains the comparison between coaxial excitation and TEA discharge.

The Ar_2F^* radiation showed an apparent peak when the F_2 pressure varied. Then, it began to decay (see Figure 5). From the decay rates of Ar_2F^* at various F_2 pressures, the quenching rate constant of Ar_2F^* by F_2 could be derived to be $k_5 = 1.83 \times 10^{-10} \text{ cm}^3 \text{ sec}^{-1}$ (equation (13)). These data were measured under sufficient Ar pressures so that the second decay component could be suppressed. We assumed that the slow reaction produced very

little product and could be neglected under experimental conditions. The quenching rates of the binary collision of two Ar_2F^* molecules by Ar and He are $k_6 = 2.2 \times 10^{-14} \text{ cm}^3 \text{ sec}^{-1}$ and $k_7 = 0.5 \times 10^{-14} \text{ cm}^3 \text{ sec}^{-1}$, respectively. The spontaneous radiation lifetime of Ar_2F^* is $\tau_{290} = 236 \text{ ns}$ from the Stern-Volmer plot based on these data.

The quenching of Ar by collision is a secondary loss mechanism considering the value of k_6 . In view of reactions (8) and (9), increasing Ar pressure could attain a higher Ar_2F^* radiation intensity by not decreasing the ArF^* output. This concept could be proved by comparing the intensity variation of ArF^* and Ar_2F^* .

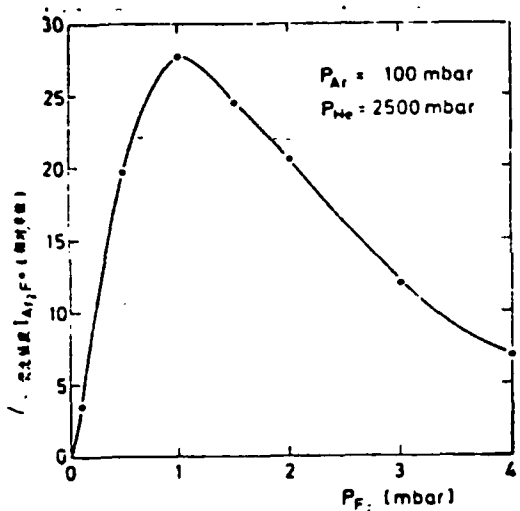


Figure 5. Ar_2F^* fluorescence radiation vs. F_2 pressure.
1--fluorescence intensity $|\text{Ar}_2\text{F}^*$ (relative unit)

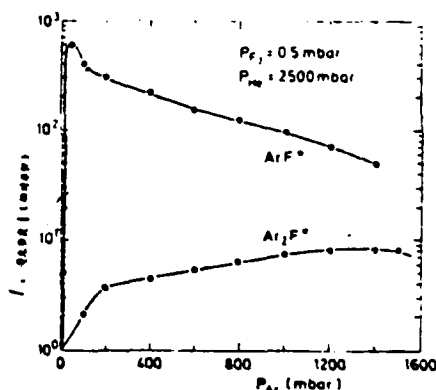


Figure 6. Radiation intensities of ArF^* and Ar_2F^* with Ar pressure.
1--fluorescence intensity $|\text{Ar}_2\text{F}^*$ (relative unit)

Conclusions

Excited quasi-molecules such as ArF^* and Ar_2F^* were formed in He-Ar-Fe mixtures by TEA discharge. The formation of Ar_2F^* is primarily through two kinetic mechanisms which are quite different in speed. The fast formation process is from the ternary reactions (8) and (9) involving ArF^* . The slow process includes the ternary reaction (5) involving Ar and the binary reaction (10) involving Ar_2^* , as well as other intermediate

steps. The relative contribution of these two sources can be controlled by the pressure ratios of the rare gases. These gas parameters can control the relative intensity at 193 nm and 290 nm. Information on the slow reaction should be obtained from time-resolved measurement of the vacuum ultraviolet radiation of Ar_2^* .

In this work, we attempted to estimate the prospect of electrically pumped Ar_2F^* lasers. The optimal parameters for this triatomic quasi-molecular fluorescent radiation can be measured. However, the loss process hindering the establishment of lasing is not yet clear to us. Because the formation mechanism is extremely complex, the absorption characteristics of many transient species are not yet known. For this reason, we hope to measure the transient absorption at 290 nm. The quenching of Ar_2F^* by electrons should also be taken into account.

/31

Experimental study on mixing GDL with a screen nozzle

Yu Gang, Zhao Jianrong, Fang Zhijia and Wu Chengkang
(Institute of Mechanics, Academia Sinica)

ABSTRACT

A small electric arc heater was used to study a $\text{CO}_2\text{-N}_2$ supersonic GDL with a screen nozzle. A 3 m^{-1} signal gain was obtained. Static and vibrational temperatures, as well as the maximum available energy, were determined. The specific power measured was 11 joules/g.

The study of modern high energy lasers is always closely related to non-equilibrium flow and fast mixing. In the development of aerodynamic lasers, a mixing gas dynamic laser not only has an efficiency much higher than that of a conventional gas dynamic laser, but also is a good experimental device to study various types of flow lasers. In a mixing gas dynamic laser,

N_2 is heated alone. CO_2 and H_2O are injected into the stream from the low temperature, low pressure area downstream and mixed with highly excited N_2 molecules. Thus, the limit that the N_2 - CO_2 gas mixture cannot exceed at the dissociation temperature of CO_2 (2300°K) in a conventional gas dynamic laser can be overcome. The useful vibrational energy ratio is significantly improved. In addition, the expansion of pure N_2 can attain a higher freeze effect to fully utilize the potential of a gas dynamic laser.

We built a 10 kg/sec flow rate, 33 kW power output combustion CO_2 laser. A screen nozzle mixing gas dynamic laser has already been put in operation. This paper describes its small signal gain, infrared radiation and power output of this device as well as static temperature, vibration temperature and maximum available energy calculated from the spectral distribution.

Experimental apparatus

Figure 1 is a sketch of the experimental apparatus. It was composed of an electric arc heater, mixing chamber, screen nozzle, optical cavity, pressure expander, heat exchanger, vacuum system and control system.

N_2 was heated by the electric arc heater. It was then expanded in the supersonic nozzle and mixed with CO_2/H_2O . The vibrational energy of N_2 molecules is transferred to CO_2 molecules, creating a population inversion in the laser cavity.

The electric arc heater was fabricated with a cerium-tungsten cathode and a copper ring anode. The power supply was a 200 kW adjustable silicon rectifier, providing power in the range of $V = 300-400$ V and $I = 100-400$ A. It met the temperature stagnation requirement. The screen nozzle was made of a block of zirconium. The nozzle area was $132 \times 20 \text{ mm}^2$. The block was filled with gas and cooling water channels (see Figure 2). There are 114 N_2 injection holes and 57 CO_2-H_2O injection holes.

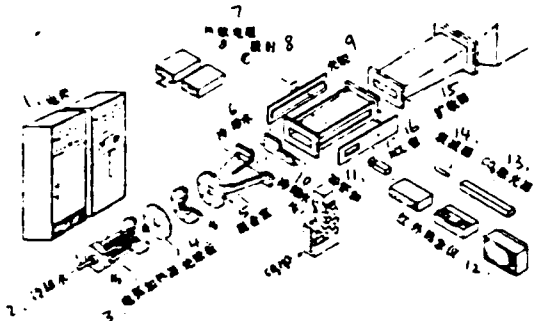


Figure 1. Experimental apparatus
 1--power supply; 2--cooling water; 3--electric arc heater; 4--insulator; 5--mixing chamber; 6--cooling water; 7--(illegible); 8--scattering; 9--(illegible); 10--cooling water; 11--nozzle; 12--infrared imaging device; 13--CO₂ laser; 14--attenuator; 15--expander

The length is 300 mm. Boundary corrections were made at the top and bottom wall. At 30, 90, 144, 96 and 350 mm away from the nozzle outlet, small signal gains were measured. The flow field was observed through a 30 x 70 mm² window. Another set of cavity heads was used for power output measurements. In order to operate for a long period of time, all hot components are actively water cooled.

Gain measurements

As shown in Figure 1, the monitoring light beam was provided by a CO₂ laser. An attenuator was used to lower the output intensity to 400 mW. The window material was potassium chloride. A thermister was used to measure the variation of the light intensity in the optical cavity to determine the gain coefficient. Figure 3 shows the distribution of small signal gain as a function of the distance from the nozzle outlet. A normalized

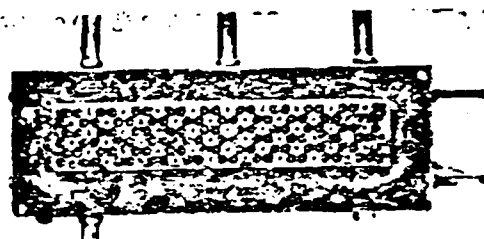


Figure 2. Photograph of the screen nozzle

The N₂ throat diameter is 0.5 mm and the angle is 10.5°. The outlet diameter is 4.5 mm (including boundary correction). The corresponding Mach number is 6. The throat height of the CO₂/H₂O injection hole is 0.5 mm and the Mach number is 4.

The cross-section area of the optical cavity is 132 x 20 mm² and

the flow field

was observed through a 30 x 70 mm² window. Another set of cavity heads was used for power output measurements. In order to operate for a long period of time, all hot components are actively water cooled.

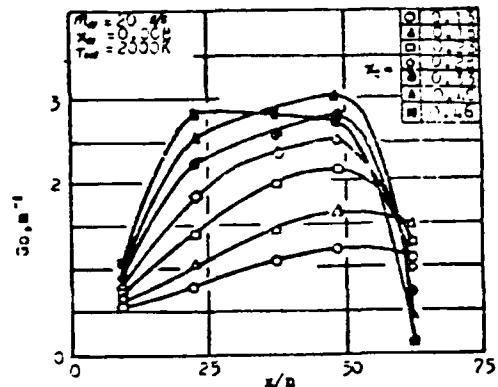


Figure 3. Distribution of small signal gain along the axis of the nozzle.

m --mass flow rate, X --gram molecular number, T_{cN} --stagnation temperature.
Subscripts N, H and C represent N_2 , H_2O and CO_2 .

away from the outlet of the nozzle is the average of several measurements. One can see that the small signal gain increases with increasing CO_2 flow rate and increasing distance from the nozzle outlet. The peak began to appear at a far away position (approximately 20 cm from the nozzle outlet). When the gram molecule of CO_2 reaches 0.40, the maximum $3/m$ was found. When the CO_2 gram molecule number reached 0.46, the gain peak shifted towards the nozzle outlet. The higher the CO_2 flow rate is, the faster the gain drops off from its peak. The reason probably is that the supersonic CO_2 molecule travels so fast that it collides with enough number of N_2 molecules only after traveling through a relatively long path. Consequently, it has the most vibrational energy possible. In addition, mixing excites CO_2 molecules. However, it also causes losses. When the CO_2 flow is relatively small with respect to that of N_2 , the flow pattern of N_2 will not be perturbed. Hence, the flow field in the cavity is basically controlled by the flow of N_2 . However, as the flow of CO_2 reaches the same order of magnitude as that of N_2 or higher, this perturbation is considerable. But, CO_2 and N_2 can be thoroughly mixed more rapidly. The peak will shift toward upstream.

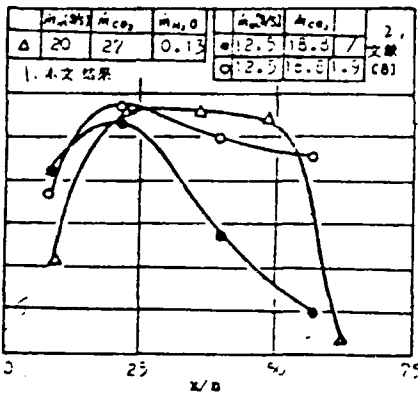


Figure 4. Comparison of small signal gains in this work to those in reference [8].

1--this work; 2--reference [8]

distance x/h was used as the horizontal coordinate where x is the distance

away from the outlet of the nozzle and h is 4 mm. The data shown in the figure is the average of several measurements. One can

see that the small signal gain increases with increasing CO_2

flow rate and increasing distance from the nozzle outlet. The

peak began to appear at a far away position (approximately 20

cm from the nozzle outlet). When the gram molecule of CO_2

reaches 0.40, the maximum $3/m$ was found. When the CO_2 gram mole-

cule number reached 0.46, the gain peak shifted towards the nozzle

outlet. The higher the CO_2 flow rate is, the faster the gain

drops off from its peak. The reason probably is that the super-

sonic CO_2 molecule travels so fast that it collides with enough

number of N_2 molecules only after traveling through a relatively

long path. Consequently, it has the most vibrational energy

possible. In addition, mixing excites CO_2 molecules. However,

it also causes losses. When the CO_2 flow is relatively small

with respect to that of N_2 , the flow pattern of N_2 will not be

perturbed. Hence, the flow field in the cavity is basically

controlled by the flow of N_2 . However, as the flow of CO_2 reaches

the same order of magnitude as that of N_2 or higher, this per-

turbation is considerable. But, CO_2 and N_2 can be thoroughly

mixed more rapidly. The peak will shift toward upstream.

Moreover, the final measurement was made at 50 mm away from the pressure expander. As the total mixture flow increases, plugging may occur. Therefore, the shock wave from the inlet of the pressure expander may re-enter the optical cavity, leading to rising static temperature and decreasing gain.

Figure 4 compares the experimental results of sonic injection in reference [1] to those in this work. Besides different CO_2 and catalyst injection speeds, other conditions are basically the same. The gain drops rapidly at sonic injection when He is absent. Supersonic injection was able to maintain a high gain over a considerably long range of distance. This is probably /33 because of the high CO_2 nozzle outlet pressure which induces a strong included shock wave. Moreover, it creates a relatively larger momentum loss. These effects will deteriorate the flow characteristics, leading to rising static temperature and decreasing gain. However, comparing to experimental data with He, the two are in good agreement. One can see that supersonic injection can lower the static temperature, at least to some extent. Figure 5 is a comparison of our data to that in reference [2]. The experimental conditions in both cases are almost identical. At the nozzle outlet, our data is lower. Considering the fact that the pressure used in reference [2] is slightly higher, it seems that higher mixture pressure may be favorable for improving the mixing process at the same flow rate.

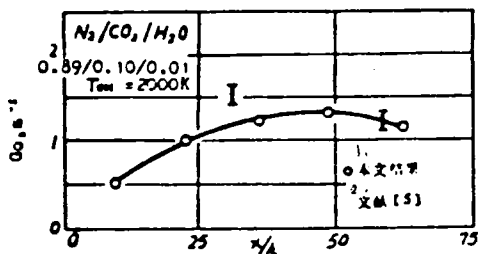


Figure 5. Comparison of small signal gains in this work to those in reference [5]

1--this work; 2--ref. [2]

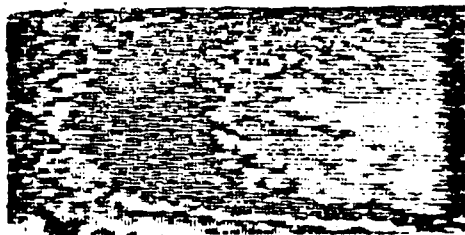


Figure 6. Radiation of excited CO_2 molecules in the optical cavity

Display of the radiation field

An infrared imaging device (developed by the Huazhong Institute of Engineering) was used to observe the radiation field of excited CO₂ molecules. Infrared radiation in the range of 8-14 μm could be displayed in different colors on the screen on a real-time, real-site basis. Furthermore, it can be recorded on magnetic tape. However, only qualitative results were obtained due to limitations in experimental conditions.

Figure 6 is a photograph of the radiation field of excited CO₂ molecules in the optical cavity (originally in color). The gas flows from left to right. The radiation intensity also becomes higher along this direction at 40 to 110 mm from the nozzle outlet. In the 80 to 110 mm range, the radiation was clearly more intense, which is in agreement with the gain measurements.

Determination of static and mean dynamic temperatures

Figure 7 shows the P branch small signal gain cross-section at 90 and 196 mm away from the nozzle outlet. The N₂ flow rate was 20 g/sec, the stagnation temperature was 2000 °K at 10 atm. Because the static pressure was around 10 torr, the line shape was corrected for Doppler effect. The line shape factor at the center of the gain curve is [3]

$$g(v_0) = \frac{2}{\pi} \left(\frac{\ln 2}{\pi} \right)^{1/2} e^{x^2} [1 - \text{erf}(x)] \quad (1)$$

where

$$\text{其中 } x = \Delta v_c \sqrt{\ln 2} / \Delta v_0, \text{ erf}(x) = \frac{2}{\sqrt{\pi}} \int_0^x e^{-t^2} dt, \quad (A)$$

Δv_c and Δv_0 are collision broadening and Doppler broadening, respectively. After neglecting the second order terms, the gain coefficient expression becomes:

$$G_n = A \frac{\lambda^2 (2j+1) \exp[-j(j+1)B/T]}{T^3} \quad (2)$$

TABLE 1. Photoluminescent peaks of undoped and Zn-doped quarternary materials from the same liquid phase composition

/39

$$X_{As}^1 = (X_{As}^1 = 0.0069, \\ 0.0550, X_{Ga}^1 = 0.0174)$$

J. 样品		4. 光发光峰值波长	5. 平均值
编号	(μm)	(μm)	
1. 不掺 Zn	UDS-07	1.51	
(本底电子浓度~	LMS-01	1.50	
$2 \times 10^{17}/\text{c.c.}$	LMS-02	1.51	1.51
	LMS-09	1.51	
	LMS-10	1.50	
2. 掺 Zn	LQ-27	1.54	
($p \sim 5 \times 10^{17}/\text{c.c.}$)	LQ-28	1.51	1.54
	DS-14	1.53	

1--undoped (background electron concentration $\sim 2 \times 10^{17}/\text{c.c.}$);
 2--Zn-doped ($p \sim 5 \times 10^{17}/\text{c.c.}$); 3--sample number; 4--photoluminescence peak wavelength (μm); 5--mean value (μm)

TABLE 2. Electroluminescence and lasing wavelengths of a typical $1.55 \mu\text{m}$ laser at room temperature.

1. 编号	2. 电荧光峰值波长 (μm)	3. 激射波长 (μm)	4. 备注
LQ-030	1.54	1.56	5. 脉冲激光
LQ-035	1.54	1.56	6. 脉冲激光
LQ-047	1.56	1.56	7. 脉冲激光
LQ-048	1.55	1.55	8. 室温连续激光

1--number; 2--electroluminescence peak wavelength; 3--lasing wavelength; 4--remarks; 5--pulse laser; 6--pulse laser;
 7--pulse laser; 8--room temperature continuous working laser

the quarternary layer with respect to the InP layer. Figures 3 and 4 respectively show the lattice mismatch of the active layer and the re-dissolution resistant layer as a function of the number of As atoms. From these curves, the "zero mismatch" active layer composition was determined to be $X_{As}^1 = 0.0174$, and $X_{As}^1 = 0.0550$. The liquid composition of the re-dissolution resistant layer is $X_{As}^1 = 0.0072$, and $X_{As}^1 = 0.0406$. Table 3 lists the experimental data points of lattice mismatch with As atom numbers. From this table, we know that the absolute lattice mismatch value is within 0.03% when a "zero mismatch" composition

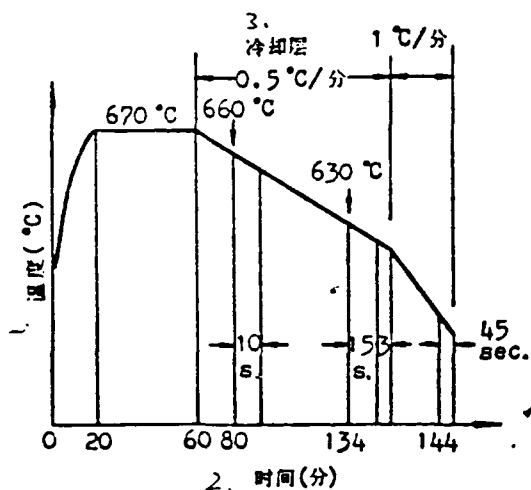


Figure 2. The epitaxial temperature program.
 1--temperature; 2--cooling layer; 3--time (min.)

reference [3] was also referred to in our work. It was experimentally determined that the liquid composition of the $1.55\text{ }\mu\text{m}$ active layer grown at 631°C should be $X_{\text{Ga}}^1 = 0.0069$, $X_{\text{In}}^1 = 0.0550$, $X_{\text{As}}^1 = 0.0174$. Table 1 shows the fluorescent characteristics of undoped and Zn-doped materials. It was estimated that the Zn acceptor level is approximately 16 MeV from the top of the valence band of the $1.55\text{ }\mu\text{m}$ active layer. This value is essentially in agreement with that in reference [4]. Table 2 shows the typical electroluminescence wavelength and lasing wavelength of a laser thus fabricated. From Table 2, we know that the composition for the active region chosen was appropriate.

2. Adjustment of the lattice compatibility of the heterogeneous InGaAsP/InP structure

In the experiment, "zero mismatch" of the quaternary liquid phase composition was realized by fixing the Ga atom number and adjusting the As atom number. Diffraction of $\text{CuK}\alpha$, X-ray on the (400) crystal surface of the epitaxial layer was used to simultaneously measure the diffraction oscillation curves of the quaternary and the InP layer. The difference of their peak diffraction angles was used to determine the incompatibility of

Several problems in liquid phase epitaxy of double heterojunction InGaAsP/InP

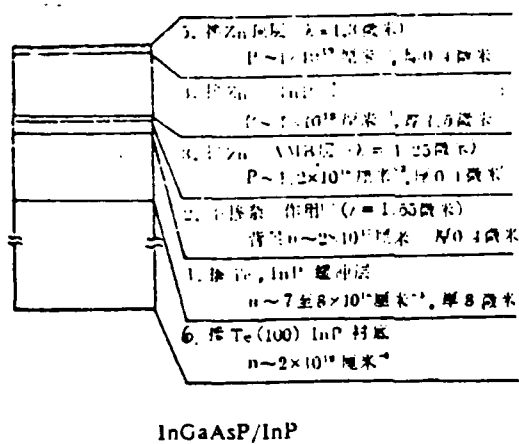
1. Selection of the liquid phase composition of the active layer

In the preparation of the epitaxial InGaAsP/InP film, the diffusion of Zn in the p type Zn-doped InP limiting layer has to be taken into account. The emitting wavelength of the laser corresponds to the transition between the conduction band of the active material and the acceptor energy level. In addition, data in

In this paper, some experimental results in the development of a $1.55 \mu\text{m}$ InGaAsP/InP proton-bombarded stripe laser were introduced, including the liquid phase composition of the active layer, the adjustment of the matching of the epitaxial lattice, the control of dopants, the fabrication of the proton-bombarded stripe laser and the laser characteristics.

Experimental

We used a two phase solution technique to grow a five layer epitaxial film with a redissolution resistant layer in a sliding graphite boat. The schematic diagram and the parameters of each layer are shown in Figure 1. The typical liquid phase growth temperature program is shown in Figure 2.



InGaAsP/InP

Figure 1. Schematic diagram of the five layer InGaAsP/InP film.

- 1--InP buffer layer doped with Te, $n=7$ to $8 \times 10^{16} \text{ cm}^{-3}$, 8 μm in thickness;
- 2--undoped active layer ($\lambda=1.55 \mu\text{m}$), background $n=2 \times 10^{17} \text{ cm}^{-3}$, 0.4 μm thick;
- 3--Zn doped AMB layer ($\lambda=1.25 \mu\text{m}$), $P=1.2 \times 10^{17} \text{ cm}^{-3}$, 0.1 μm thick;
- 4--Zn doped InP layer, $P=1 \times 10^{18} \text{ cm}^{-3}$, 1.5 μm thick;
- 5--Zn doped top layer ($\lambda=1.3 \mu\text{m}$), $P=1 \times 10^{17} \text{ cm}^{-3}$, 0.4 μm thick;
- 6--Te doped (100) InP substrate, $n=2 \times 10^{19} \text{ cm}^{-3}$

Wang Wei, Zhang Jingyuan, Tian Huiliang and Sun Furong
(Institute of Semiconductors, Academia Sinica)

ABSTRACT

A room temperature CW 1.55 μm proton-bombarded InGaAsP/InP double heterojunction (DH) laser was prepared. The minimum threshold current density was 2000 A/cm^2 at room temperature. The mean normalized threshold current density was $5000 \text{ A/cm}^2 \mu\text{m}$. The threshold characteristic temperature near room temperature was 48°K . It operated in a single longitudinal mode at 1.3 times the dc threshold.

It is well known that the transmission loss of a quartz based optical fiber is lowest in the 1.0-1.7 μm range. In this wavelength range, the most promising light source is the 1.55 μm InGaAsP/InP DH laser because the transmission loss of a single mode optical fiber has already been reduced to 0.2 dB/KM at 1.55 and that of a multi-mode optical fiber is as low as 0.29 dB/KM. It was also proven experimentally that the dispersion in the low loss wavelength range, 1.5 μm -1.6 μm , can be eliminated by appropriately reducing the core diameter of the quartz fiber and by increasing the difference in refractivity between the core and the envelope. It is useful in developing long range, high capacity optical communication systems. For this reason, although the difficulty exists in the preparation of the 1.55 μm InGaAsP/InP DH laser, people are still very interested in this wavelength device. In the preparation of 1.55 μm InGaAsP/InP by liquid phase epitaxy, the active InGaAsP/InP layer might be dissolved by the solution to grow the limiting InP layer. This is especially true when a low temperature and supercooling method was used to grow a redissolution resistant structure. In recent years, in order to lower the threshold current and to achieve stable single mode or multi-mode operation, several 1.5 μm -1.6 μm stripe InGaAsP/InP DH lasers were developed [1-2].

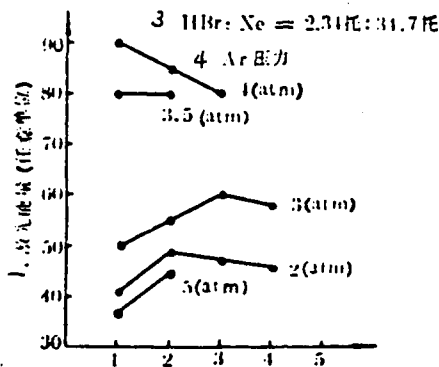


Figure 8. Relationship between XeBr laser energy and number of pulses.

1--laser energy (arbitrary unit); 2--pulse number; 3--HBr: Ne = 2.34 torr = 34.7 torr; 4--Ar pressure

Our laser was pumped uniformly by an intense electron beam. It operated far above the threshold value. When operating at high pressures, the following reactions might take place: $Xe + e \rightarrow Xe^* + Xe$, $Xe^* + Br \rightarrow XeBr^* + Br$ to enhance the formation of $XeBr^*$ at a specific Xe pressure. It also reduced the absorption loss due to Xe_2^+ . High pressure XeBr lasers can be realized by choosing an appropriate HBr concentration (1.4-2.4 torr) to minimize the absorption loss by HBr.

Homogeneous intense pumping, constant Xe pressure, and a suitable HBr concentration are the conditions for high pressure XeBr lasers to come true.

References:

[1] J. J. Ewing et al., A.P.L., 28, 656 (1976).

High pressure XeBr laser

High pressure XeBr laser oscillation at 282 nm was realized when the gas ratios were HBr:Xe:Ar = 2.3 torr:34.7 torr:2-5 atm. The energy output was close to 1.7 mJ. Figure 7 shows the dependence of the laser energy output in Ar pressure at fixed HBr:Xe = 1.15 pressure ratio under constant excitation. The optimal Ar pressure range is 3.5-4 atm. Figure 8 shows the relation between laser energy output and pulse number at various Ar pressures. The optimal Ar pressure for slow output energy attenuation is 3.5 atm.

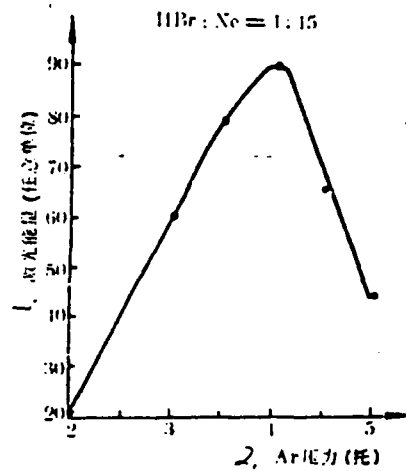
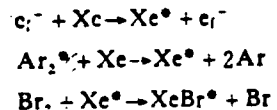


Figure 7. XeBr laser energy vs. Ar pressure. 1--laser energy (arbitrary unit); 2--Ar pressure (torr)

The laser spectrum obtained by the spectrophotometer indicates that the center frequency is 2820.69 Å. The half width $\Delta\lambda = 4.29 \text{ \AA}$.

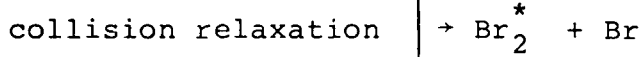
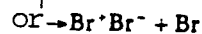
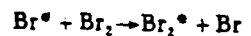
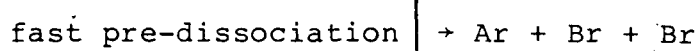
XeBr is formed according to the following reactions:



Because there are many absorption losses in the XeBr system, high pressure operation is affected. For example, there are (1) the absorption loss of the XeBr photon (35460 cm^{-1}) due to the continuous absorption band of $A \rightarrow x$ by HBr, which limits the concentration of HBr, (2) the resonance absorption loss of the XeBr photon by the energy level of $XeBr^*$ dissociation, and (3) the absorption loss by Xe_2^* and Xe_2^+ as produced by the electron beam excitation. The absorption loss of Xe_2^* and Xe_2^+ increases proportionally with the square of pressure.

At high pressures, the absorption loss due to Xe_2^* and Xe_2^+ is further increased. The XeBr laser beam operating near the threshold was terminated.

(2) Molecular reactions



(3) Atomic reactions: at high pressures



The major conduits are ion recombination and molecular reactions

Discussion

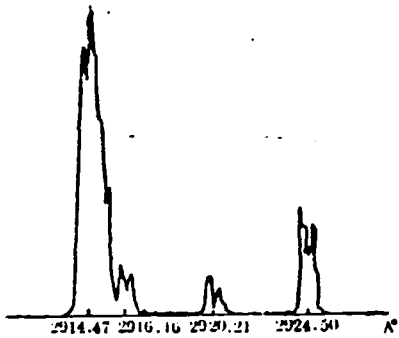


Figure 6. Br_2^* laser spectrum.

(1) It was discovered experimentally that the efficiency and operating lifetime of the laser could be improved by increasing the HBr concentration: This is because an increase in HBr concentration: (1) could effectively quench the B state particles weakly bound at the laser energy level to alleviate the bottleneck effect.

(2) The Br density was increased to enhance the reactions for Br_2^* formation. (3) The optimal gas composition was maintained by compensating the contamination of the cavity wall by HBr.

In order to minimize HBr consumption, the suitable pressure of HBr is 7-8 torr.

(2) It was also discovered in our experiment that in a HBr-Ar system the first operation required the excitation of an electron beam in order to produce an intense laser beam in subsequent excitations. The pre-excitation is primarily to dissociate HBr into Br and Br_2 to induce various reactions in the gas mixture. It promotes the mixing of gases to lower the threshold of excitation.

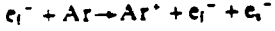
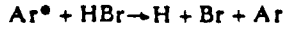
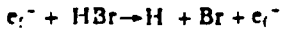
Figure 2 shows the dependence of laser energy on Ar pressure at constant excitation. The optimal Ar pressure is 3 atm. Figure 3 shows that the optimal HBr pressure range is 5.6-8 torr at constant Ar pressure and excitation. Figure 4 shows that the energy decays rapidly and the operating lifetime is shortened when HBr < 5 torr. When HBr > 5.6 torr, the energy output is high. The decay is slow and the operating lifetime is long (see Figure 5).

The relative darkness curve of the Br_2 molecular laser spectrum as measured by a 2 m spectrophotometer is shown in Figure 6. We obtained four intense lasing lines : 2914.47 \AA , 2916.16 \AA , 2920.21 \AA and 2924.50 \AA . 2916.16 \AA was not reported in reference [1].

Formation mechanism of Br_2^* molecules

Excited Br_2^* molecules are created through energy transfer from highly excited Ar^* and Ar_2^* molecules. In analogy to I_2 and noble gas halides, Br_2^* molecules may be formed by three primary reactions:

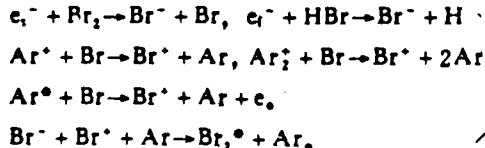
The formation of Br and Ar in various states (e_f^- is a high energy fast electron and e_s^- is a secondary electron):



Ar_2^+ , Ar^* and Ar_2^* are formed by collision at high pressures.

/36
/37

(1) Ion recombination



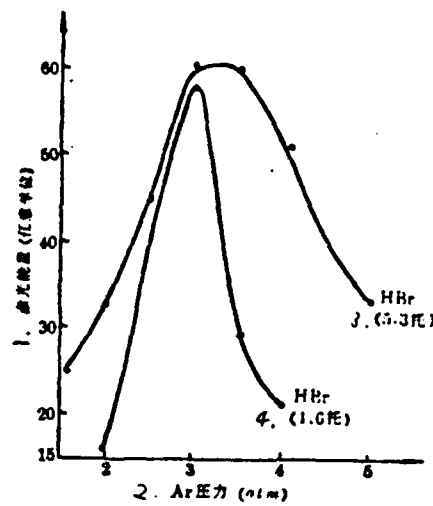


Figure 2. Br_2 laser energy vs. Ar pressure.
1--laser energy (arbitrary unit); 2--Ar pressure; 3--(5.3 torr);
4--(4.6 torr)

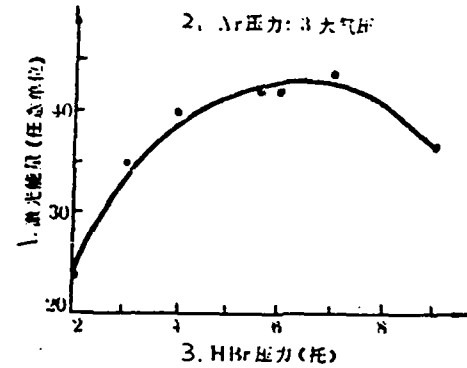


Figure 3. Br_2 laser energy vs. HBr pressure.
1--laser energy (arbitrary unit); 2--Ar pressure:
3 atm; 3--HBr pressure; 4--HBr (4.6 torr)

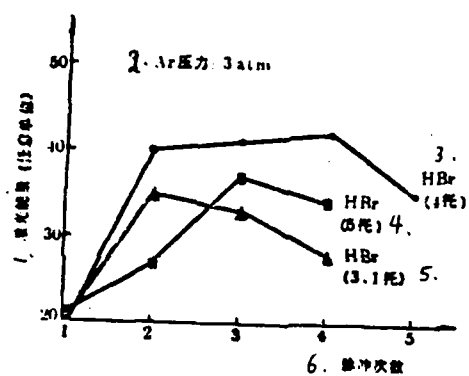


Figure 4. Br_2 laser energy vs. number of pulses (HBr pressure < 5 torr).
1--laser energy (arbitrary unit); 2--Ar pressure:
3 atm; 3--(4 torr); 4--(5 torr); 5--(3.1 torr);
6--number of pulses

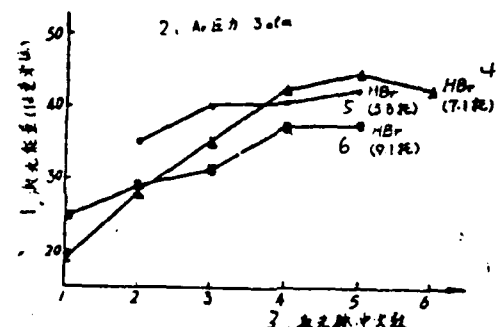


Figure 5. Br_2 laser energy vs. number of pulses (HBr pressure > 5 torr).
1--laser energy (arbitrary unit); 2--Ar pressure:
3 atm; 3--number of laser pulses; 4--(7.1 torr);
5--(5.6 torr); 6--(9.1 torr)

Furthermore, the operating lifetime and efficiency of the laser was improved by raising the HBr concentration. (2) In a HBr-Xe-Ar mixture, the high pressure operation of XeBr at 282 nm in the 2-5 atm pressure range was realized for the first time. Furthermore, the high pressure operating mechanism was discussed.

The experimental apparatus is shown in Figure 1. The relativistic electron beam was generated by a Marx high voltage generator and a field emission diode. The cathode was made of three 0.12 mm thick knife shaped titanium foils spaced at 1 mm apart. The anode is a 0.015 mm thick titanium foil window. The electron beam energy was measured to be 1.12 MeV. The electron beam current was 6 KH. The pulse width (full width at half weight) is 25 ns. The rising leading edge is < 8 ns. This electron beam was injected transversely into a (10×70) mm² window of the stainless steel laser box. The laser cavity was 15 cm long and 16 mm in diameter. A quartz plate coated with a dielectric film and a plane-plane cavity structure were used. At 282 nm and 292 nm, the reflectivity of the mirror $R = 99\%$. The transmittance of the output coupling lens $T = 6\%$. A carbon funnel was used to measure the laser energy output. The Fe spectrum was used to determine the laser wavelength by use of a 2m grating spectrophotometer 3 meters away from the output end of the laser.

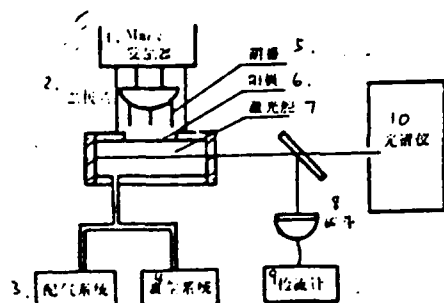


Figure 1. Schematic diagram of the apparatus.
 1--Marx generator; 2--diode;
 3--gas mixing system; 4--vacuum system;
 5--cathode; 6--anode; 7--laser cavity;
 8--alkaline funnel; 9--flow detector; 10--spectrophotometer

Br_2^* molecular laser

/36

Laser oscillation of Br_2^* molecules at 292 nm due to $E \rightarrow B$ transition was realized in a HBr-Ar gas mixture when the gas ratio is HBr:Ar = 5 atm: 3 atm. The energy output was measured to be 1.12 mJ and the operating pressure range was 2-5 atm.

unit mass of medium based on the E_{\max} calculated from the gain measurement.

Comrades Li Chunjin, Li Jianguo, Zhang Liang, Zhao Dufeng, Liu Houkuan, Wu Chuanbao, Fan Qingling, Zhu Mingfa and Zhuang Tao. We wish to express our gratitude to the electric arc heater group of the 11th Laboratory in the Institute of Mechanics.

References

- [1] H. Hugel et al: [3d, Int. Symp. on Gas-Flow and Chem. Lasers. Cg-335, (1980).
- [2] P. E. Cassady, et al: AIAA paper, №. 76-343, (1976).
- [3] T. Coor: J. Appl. phys., 40, 3563 (1969).

/35

1 MeV REB pumped Br_2^* molecular laser and high pressure XeBr laser

Wang Chanshan, Chen Yongrong, Xu Zhihai
(Anhui Institute of Optics and Fine Mechanics, Academia Sinica)

ABSTRACT

A 1 MeV relativistic electron beam (REB) was used transversely to pump a HBr-Ar mixture to realize for the first time four intense laser lines of Br_2 molecules near 292 nm. In the 2-5 atm pressure range, XeBr oscillation at 282 nm was materialized. The laser characteristics were discussed.

Until now, a Br_2^* molecular laser was realized in a Br_2 -Ar system and XeBr lasers were operating at below 2 atm.

We used a 1 MeV REB transversely to pump the laser. HBr was used as the bromine donor. (1) A lasing oscillation (operating in the 2-5 atm range) was realized for the first time in a HBr-Ar mixture. It is the $E \rightarrow B$ band transition of Br_2^* molecules at 292 nm. It was proven to be effective to realize the Br_2^* molecular laser transition in the HBr-Ar system.

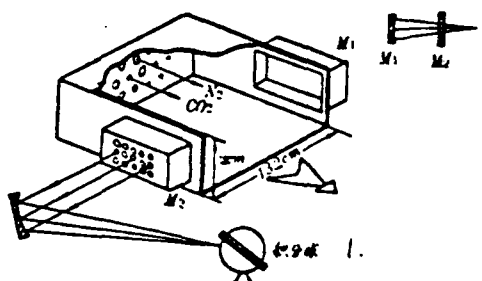


Figure 8. Structure of the cavity.
1--spherical integrator

The coupling was 8%. The reason for this discrepancy is that the area of the rectangular lens used in multi-hole coupling is larger than that of the round mirror used in single hole coupling (by approximately 60%).

When the stagnation temperature of N_2 increased from 1500 °K to 2000 °K, the power output rose from 160 watts to 220 watts correspondingly (see Figure 10). It was also discovered in the experiment that the catalyst-water was not effective. Some Ar was used to replace N_2 in order to lower the static temperature in the cavity to improve the power output. However, the effect was insignificant. This might be because the stagnation temperature of N_2 was not high enough.

/42

In our small scale experimental device, the advantages of a mixing gas dynamic laser are fully demonstrated. The specific power reached 11 joule/g with relatively low mirror losses and less than optimal coupling. This is already much higher than that of our previous pre-mixed gas dynamic laser (3.3 joule/g). If the gas mixing characteristic can be further improved and a suitable resonance cavity and high mass reflective mirror are chosen, it is hopeful to obtain 20-25 joule/g of energy from a

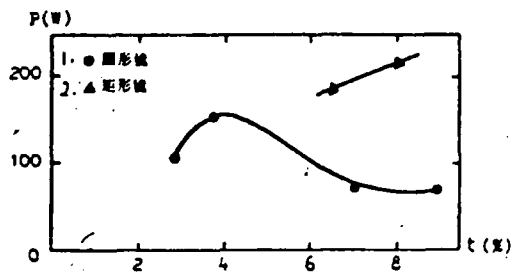


Figure 9. Variation of power output with coupling.
1--round lens; 2--rectangular lens

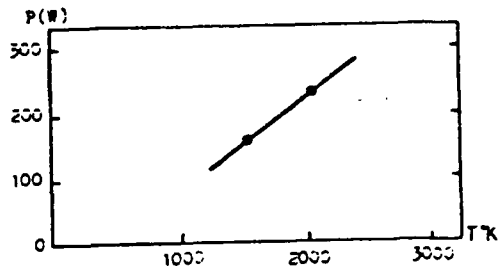


Figure 10. Variation of power output with stagnation temperature.

The maximum effective laser energy can be calculated from the vibrational temperature and mean dynamic temperature according to:

$$E_{max} = \eta \frac{R\theta_1}{M} (x_C + x_N) \left(\frac{1}{e^{E_1/T_1} - 1} - \frac{1}{e^{E_2/T_2} - 1} \right)$$

where $\eta = 0.409$ which is the quantum yield of the 10.6 micron CO_2 laser transition. x_C and x_N are the gram molecules of CO_2 and N_2 , respectively. M is the average gram molecules of the laser medium. The maximum energy attainable from a good optical cavity is approximately 70% of E_{max} . Therefore, it was estimated that the maximum energy of the device should be about 30 joule/g at its maximum gain.

Measurement of power output

A stable cavity structure such as the one shown in Figure 8 was used. Its optical axis is located in the region between 11 to 19.5 cm from the nozzle outlet. The resonance cavity was made of convex copper-beryllium reflective mirrors and a planar output mirror with holes. The mirror may have a single hole or many holes. In order to avoid the sputtering particles of the electric arc heater carried in the N_2 gas from damaging the mirrors, the mirror surface was recessed from the wall surface by about 5 cm. Even so, the reflectivity was reduced from 96% before the experiment to 92% after the experiment. The window material is Kcl. Its transmittance is 94%.

The laser output was measured by a spherical integrator. It was calibrated against burning plexiglass. The latter can only provide the average power. The peak power is approximately 1.5-2.0 times the average power. Figure 9 shows the measured results. The data was obtained when the N_2 stagnation temperature was 2000 °K and the gram molecules of the gas mixture were 0.4 CO_2 /0.6 N_2 . The maximum power output was 150 watts with single hole coupling. The corresponding coupling is 3.6%. The maximum power output is 220 watts with multi-hole coupling.

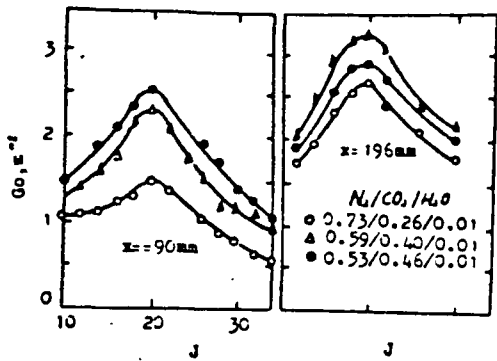


Figure 7. Distribution of P branch small signal gain with j

and ν_3 vibrational modes of CO_2 , respectively. τ is the radiation lifetime and R is the gas constant. M_{CO_2} and N_{CO_2} are the gram molecular number and particle density of CO_2 , respectively. Because of the fast relaxation between energy levels, $T = T_1 = T_2 = \text{constant}$. After we rendered equation (2) dimensionless and took the logarithm on both sides, it became a linear equation:

$$\ln \left[\frac{\lambda_0^2 G_0}{\lambda_j^2 (2j+1)} \right] = \ln \left[\frac{A \lambda_0^2}{T_1^2} \right] - j(j+1) \frac{B}{T} \quad (4)$$

where λ_0 was introduced by the dimensionless treatment. λ_0 might be chosen to be 10.6 micron. Equation (4) is a straight line if $\ln \left[\frac{\lambda_0^2 G_0}{\lambda_j^2 (2j+1)} \right]$ and $j(j+1)$ are used as the vertical and longitudinal coordinates. Its slope and intercept are T and T_3 , respectively. The results are listed in Table 1.

TABLE 1. Static temperature, vibrational temperature and maximum effective laser energy

CO ₂ 1. 克分子数	2. 90 毫米			3. 196 毫米		
	T(K)	T ₃ (°K)	E _{max} (焦耳/克)	T(K)	T ₃ (°K)	E _{max} (焦耳/克)
0.26	312	1158	19.5	346	1638	50.4
0.40	336	1220	21.1	361	1570	42.0
0.46	354	1232	20.7	382	1512	36.5

1--gram molecules; 2--90 mm; 3--196 mm; 4--E_{max} (joule/gram);
5--E_{max} (joule/gram)

$$A = \frac{B \tau^2 [1 - \text{erf}(x)]}{4 \sqrt{2 \pi^2 \tau^2 R / M_{\text{CO}_2}}} N_{\text{CO}_2} \cdot [e^{-\theta_3/T_3} - e^{-\theta_1/T_1}] [1 - e^{-\theta_1/T_1}] \cdot [1 - e^{-\theta_2/T_2}]^2 [1 - e^{-\theta_3/T_3}] \quad (3)$$

Here, λ_j is the radiation wavelength, j is the quantum number of the laser energy transition, B is the rotational constant, and T is the rotational temperature.

θ_1 , θ_2 , θ_3 and T_1 , T_2 , T_3 represent the characteristic vibration temperatures and energies (expressed as temperatures) of the ν_1 , ν_2

and ν_3 vibrational modes of CO_2 , respectively. τ is the radiation lifetime and R is the gas constant. M_{CO_2} and N_{CO_2} are the gram molecular number and particle density of CO_2 , respectively.

Because of the fast relaxation between energy levels, $T = T_1 = T_2 = \text{constant}$. After we rendered equation (2) dimensionless and took the logarithm on both sides, it became a linear equation:

$$\ln \left[\frac{\lambda_0^2 G_0}{\lambda_j^2 (2j+1)} \right] = \ln \left[\frac{A \lambda_0^2}{T_1^2} \right] - j(j+1) \frac{B}{T} \quad (4)$$

where λ_0 was introduced by the dimensionless treatment. λ_0 might be chosen to be 10.6 micron. Equation (4) is a straight line if $\ln \left[\frac{\lambda_0^2 G_0}{\lambda_j^2 (2j+1)} \right]$ and $j(j+1)$ are used as the vertical and longitudinal coordinates. Its slope and intercept are T and T_3 , respectively. The results are listed in Table 1.

is selected. The table also lists the lattice mismatch data at the top of the InGaAsP layer. Considering the trend that the lattice constant increases when the liquid phase composition remains unchanged and the growth temperature decreases, the composition of the "zero mismatch" top layer was experimentally determined by interpolation to be $X_{Ga}^1 = 0.0072$, and $X_{As}^1 = 0.0398$, using the composition of the re-dissolution resistant layer as the basis. Figure 5 shows the diffraction oscillation curve of the quintuple structure when the three quarternary layers were grown using the "zero mismatch" composition. The overall absolute lattice mismatch is less than 0.04%.

/40

TABLE 3. Experimental data on lattice compatibility

层别	样品 2.	液相组分(%) ³	晶格失配度 ⁴	
	编号	X_{Ga}^1	X_{As}^1	$\Delta a_1/a_1$
5 有源层	LMS-09	1.74	5.45	-5.5×10^{-4}
	LMS-12	1.74	5.50	$+2.7 \times 10^{-4}$
	LMS-02	1.74	5.55	$+9.2 \times 10^{-4}$
6. AMB层	LMS-10	1.74	5.65	$+2.0 \times 10^{-3}$
	LMS-07	0.72	3.91	-3.2×10^{-3}
	LMS-03	0.72	3.99	-1.6×10^{-3}
	LMS-04	0.72	4.01	-1.6×10^{-3}
	LMS-11	0.72	4.06	$\pm 2 \times 10^{-4}$
7. 顶层	LMS-06	0.72	4.11	$+9 \times 10^{-4}$
	LMS-13	0.72	3.95	-8×10^{-4}
	LMS-11	0.72	3.98	$+3.3 \times 10^{-4}$
	LMS-16	0.72	4.01	$+8.8 \times 10^{-4}$

1--layer; 2--sample number; 3--liquid phase composition (%);
4--lattice incompatibility; 5--active layer; 6--AME layer;
7--top layer

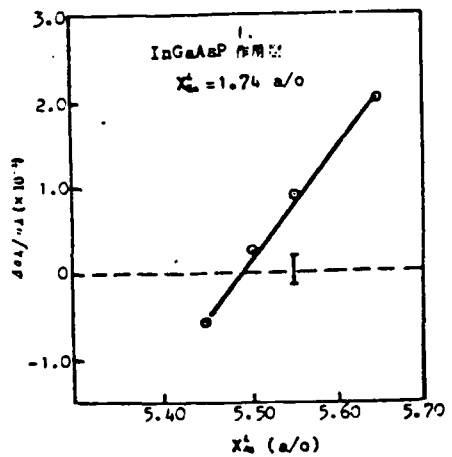


Figure 3. Lattice mismatch in the active layer vs. As atom number.
1--active InGaAsP layer

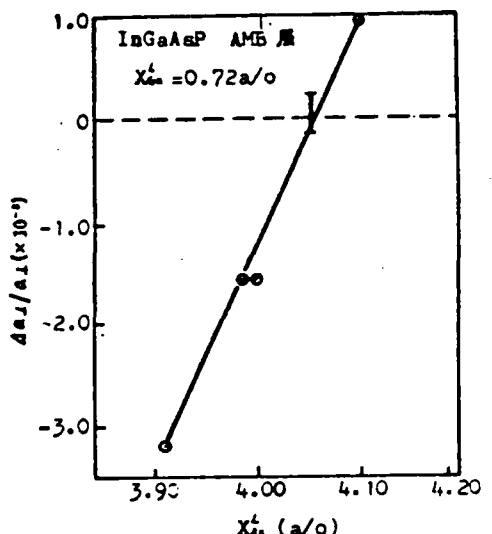


Figure 4. Lattice mismatch in the re-dissolution resistant layer vs. As atom number.
1--AMB layer

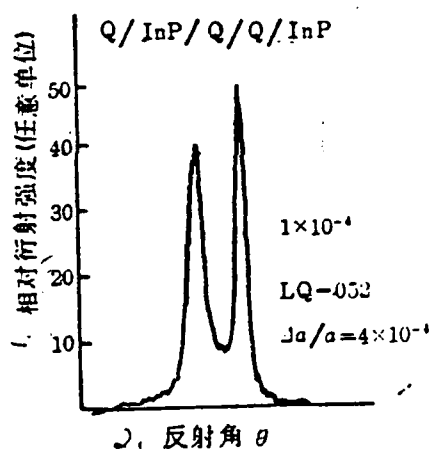


Figure 5. X-ray diffraction oscillation curve of the quintuple epitaxial film.

1--relative diffraction intensity (arbitrary unit);
2--reflection angle θ

Although the active layer was not intentionally doped, yet the fast diffusing impurity Zn would diffuse into the active layer from the re-dissolution resistant layer in the liquid phase epitaxy process. It was even diffused into the InP buffer layer. Therefore, it is very important to control the doping of Zn. The amount of Zn chosen for doping the re-dissolution layer is considered as follows:

(1) Usually, undoped quaternary layers are n-type due to Si contamination.

(2) In order to avoid the formation of a far junction, the Te doping level in the InP buffer layer should be sufficiently high ($n = 7 \times 10^{18} / \text{c.c.}$ was chosen by us) to ensure the position of the p-n junction is terminated at the heterojunction between the active layer and the InP buffer layer. /41

(3) Since the doping of the n-type InP buffer layer is sufficiently high, this layer is already degenerated. If the p-type active layer is highly doped and degenerated, a tunneling effect will appear. This does not favor radiation recombination. Therefore, the active layer must be suitably doped.

(4) Assuming that the diffusion of Zn from the re-dissolution layer to the active layer satisfies the semi-infinite diffusion model so that the Zn concentration at the interface between the re-dissolution resistant layer and the active layer is always maintained at 1/2 of that in the re-dissolution resistant layer, the Zn concentration in the active region becomes closer to that near the interface as the diffusion time gets longer.

Based on the above and assuming all the Zn dopant is electroactive, then the net hole concentration in the active region N_A is:

$$N_A = N_A/2 - N_D \quad (1)$$

N_A represents the amount of Zn doped into the re-dissolution resistant layer. N_D represents the background electron concentration of the active layer. The value of N_D in the $1.55 \mu\text{m}$ active region was measured to be $2 \times 10^{17} / \text{cm}^3$. By choosing $N_A = 1.2 \times 10^{18} / \text{cm}^3$, then N_A was estimated to be $4 \times 10^{17} / \text{cm}^3$ based on equation (1). In order to verify this result, we carried out C-V measurements with a $1.55 \mu\text{m}$ proton-bombarded stripe laser (see Figure 6). The strict linear relation between $1/C^2$ and V show that the p-n junction is an abrupt junction. The intercept on the bias axis is $V_D = 0.79 \text{ V}$, which corresponds to the band gap width of the $1.55 \mu\text{m}$ quarternary material. This indicates that the experimental data is convincing. The relation

between the junction capacitance and the low concentration carrier concentration N_a of an abrupt heterojunction is:

$$N_a = \frac{2(V_b - V_0)}{\epsilon \epsilon_0} \left(\frac{C_j}{A} \right)^2 \quad (2)$$

where V_b is the added bias, ϵ_a is the dielectric constant of the active region and A is the area of the p-n junction. From the slope in Figure 6, N_a was calculated to be $5 \times 10^{17} / \text{cm}^3$ based on equation (2), which is essentially in agreement with the predicted value based on equation (1).

Fabrication and characteristics of the 1.55 μm proton-bombarded stripe laser

The five layer epitaxial film described above was reduced to 100 μm thickness. The p and n surfaces were evaporated with Au/Zn/Au and Au-Ge-N, respectively, as electrodes. A 15 μm diameter tungsten wire was used as the shield for proton-bombardment to become a proton-bombarded stripe. The bombarding energy was 200 KeV and the dose was $3 \times 10^{15} / \text{cm}^3$. It was cleaved into a 250 μm long and 300 μm wide chip. The p-type surface was facing down and in contact with a In coated copper heat sink. The optoelectric characteristics of this device are as follows:

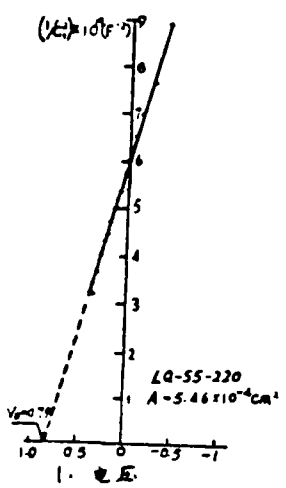


Figure 6. Capacitance-voltage characteristic of a typical proton-bombarded stripe laser. C -- capacitance

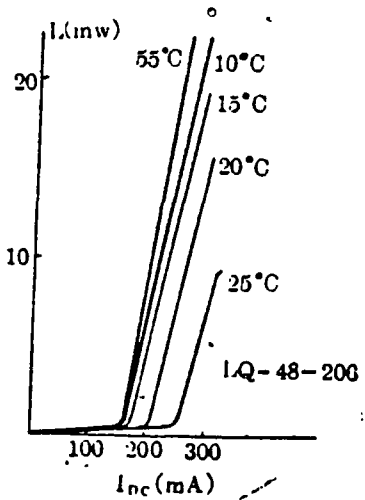


Figure 7. Light intensity-current relation of the proton-bombarded stripe laser at various heat temperatures

1. Under pulsing conditions (pulse width 1 μ s, repetition frequency 10 KC), the room temperature threshold temperature density is usually 3-4 KA/cm^2 . The lowest was 2000 A/cm^2 , corresponding to a normalized threshold current density of 5-6 $\text{KA}/\text{cm}^2 \cdot \mu\text{m}$.

2. Figure 7 shows the relation between the single face power output and dc injection current of a typical proton-bombarded stripe laser at various heat sinking temperatures. At 20°C, the threshold current is 200 mA.

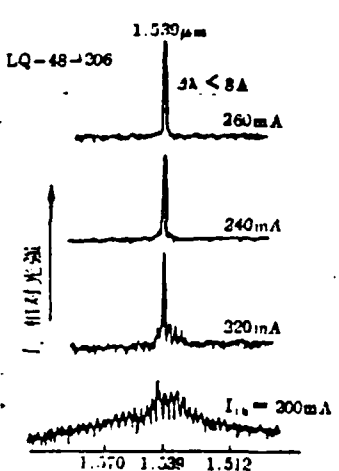


Figure 8. Room temperature laser spectrum of a typical proton-bombarded stripe laser.
1--relative light intensity

3. Figure 8 shows the laser spectrum continuously operating at room temperature. When the current is increased to 1.3 times the threshold value, the spectrum is in a single longitudinal mode. The laser wavelength is 1.539 μm .

4. The threshold current-temperature relationship of a typical device was measured in low repetition frequency, narrow pulse width conditions. From Figure 9, we know that this

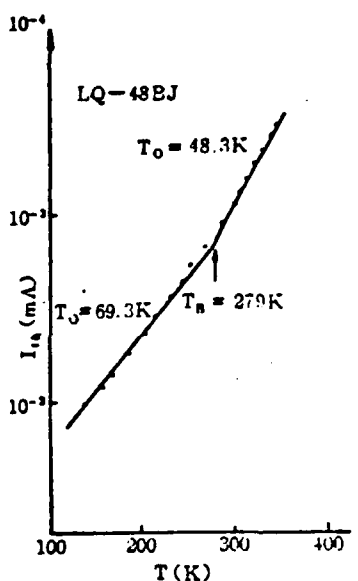


Figure 9. Threshold current vs. temperature for a 1.55 μm proton-bombarded stripe laser

relation obeys the $I_i(T) \propto \exp(T/T_0)$ law. Experimentally, it was determined that the deflection temperature $T_B = 279^\circ\text{K}$. The characteristic temperature T_0 of the threshold current below T_B is 70°K .

Comrade Duan Shushen participated in the early stage of this work. Assistance from comrades Gao Jilin, Wang Xiaoqie, Xu Junying, Xu Jizong, Gong Jishu, Jiang Sinan, Wang Wannian, He Guangping, Xu Xuemin, Ge Yuru and Wang Wang Weiming was appreciated.

References

- [1] I. Mito: Electron lett., 18, No 1, 2 (1982)
- [2] H. Imai: Fujitsu Sci. Tech. J. 18, 4 (1982)
- [3] S. Arai: IEEE J. Q. E., QE-16, 197 (1980)
- [4] Y. Yamazoe: Japan J. A. P., 19, Sapple-
memt 19-2, 207 (1980).

Investigation on frequency stability of dye lasers

/43

Yan Bingyu
(Beijing Institute of Opto-electronics, Beijing)

ABSTRACT

The variation of dye laser beam direction was studied using a specially designed interferometer and a servo system. It was compensated to improve the frequency stability of stable frequency dye lasers.

In order to attain a higher resolution spectrum, the frequency of a dye laser is usually stabilized at one of the resonance frequency of an optical resonance cavity. The dye laser frequency is usually fixed at the half width point S of the transmission curve of the reference cavity, as shown in Figure 1. 4% of the laser beam is fed into the reference cavity through mirrors and a telescope. The attenuator is so adjusted

that I_{Ref} is one half of the transmitted peak value I_{res} . It means that $I_{res}(f) - I_{Ref} = 0$ or $I_{Ref}(f) = I_{res \ max}/2$. If the frequency of the dye laser changes so that this signal difference is not equal to zero, it will be amplified and fed back to the ADP (opto-electronic modulator) in the cavity, or to the PZT (piezo electric ceramic) on the mirror in the cavity, to change the length of the resonance cavity. Consequently, the output frequency is changed. However, if the beam direction of the dye laser changes, then the mode varies in the reference cavity. The operating point is shifted from S to S' to cause a frequency change Δf . This frequency change cannot be controlled by the frequency stabilizing system. Consequently, an additional frequency noise is introduced to the dye laser.

In this paper, the effect of the directivity of the laser beam on frequency stability was calculated first. Next, a specially designed interferometer was used to measure the variation of laser beam direction. An electronic servo system was used to stabilize the output direction to improve the frequency stability of the laser.

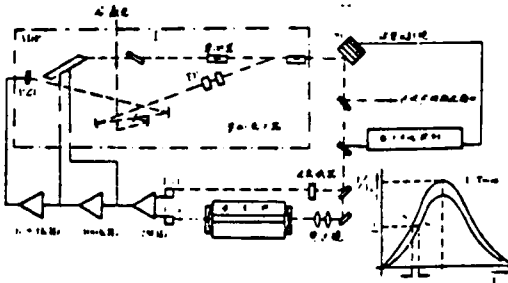


Figure 1. Principle of frequency stabilization of dye lasers (writing inside figure illegible)

Theory

1. Computation of reference cavity mode and matching beam parameters

In order to calculate the mode change in the reference cavity due to changes in the laser beam direction, it was

necessary to calculate the optical parameters matching the reference cavity mode. If the reference cavity parameters are that: the radius of curvature of the concave mirror $r_1 = 300$ mm, the distance between the concave mirror and the plane mirror $d = 230$ mm (see Figure 2) and the reflectivity of the mirrors $R = 0.99$, then

$$\bar{Z}_0 = \{d(r_1 - d)\}^{1/2} = 126.9 \text{ mm}$$

$$\bar{W}_0^2 = \frac{\lambda}{\pi} \cdot \bar{Z}_0 = 0.0265 \text{ mm}^2$$

$$\bar{W}_0 = 0.1629 \text{ mm} \quad \text{with respect to} \quad \lambda = 657 \text{ nm}$$

$$\text{The divergent angle } \bar{\gamma} = \bar{W}_0 / \bar{Z}_0 = 1.28 \times 10^{-3}$$

/43

/44

2. Coupling parameter of an oblique incident reference cavity

An incident Gaussian light beam may be expanded as the characteristic function of the resonance chamber:

$$\psi^{(0)}(x, y, z) = \sum_{m,n=0} k_{mn} \psi_{mn}(x, y, z)$$

when k_{mn} is the excitation or coupling coefficient of the characteristic function ψ_{mn} . Because of the high reflectivity of the mirror in the reference cavity and the appropriately chosen distance between the mirrors, only the sharp transmission maximum was observed in tuning the reference cavity. Therefore, only the coupling coefficient of the basic wave k_{00} is needed. In the case of oblique incidence, the coupling coefficient of the basic characteristic wave in the resonance chamber is given by the following formula (see Figure 3). $|k_{00}|^2 = \exp \left[-\frac{1}{W_0^2} \left(x_1^{(0)} + y_1^{(0)} \right)^2 - 2 x_1^{(0)} \bar{Z}_0 \sin \gamma + (\bar{Z}_0^2 + \bar{Z}_1^2) \sin^2 \gamma \right]$

$$- 2 x_1^{(0)} \bar{Z}_0 \sin \gamma + (\bar{Z}_0^2 + \bar{Z}_1^2) \sin^2 \gamma \right]$$

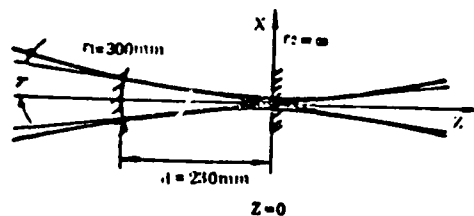


Figure 2. Reference resonance cavity parameters and profile of mode matching light beam

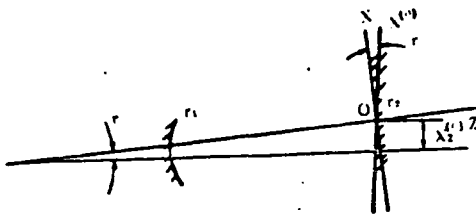


Figure 3. Definition of parameters of an obliquely incident laser reference cavity at an angle γ

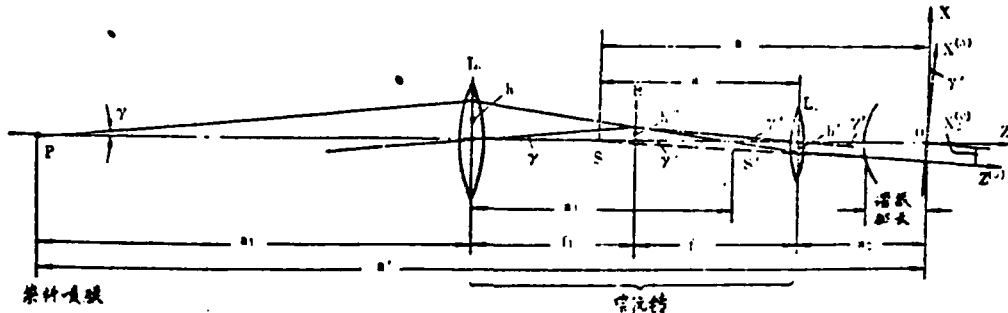


Figure 4. Relation between reference cavity. Telescope and dye laser beam at an angle γ (P: point of inclination on the dye film, S: effective point of inclination of the incident reference cavity and the angle of inclination γ)

The optical axis in the reference cavity coincides with the z axis in the x,y,z coordinate. The coordinate is rotated by an angle γ to form a new coordinate system; $x^{(0)}, y^{(0)}, z^{(0)}, x_i^{(0)}, y_i^{(0)}$ represent the distance of the oblique incident beam in the coordinate system. Assuming that the direction of the dye laser only changes on a certain plane, a' is the distance between the dye film to the rear mirror of the reference cavity, and γ is the angle between the dye laser beam on the x,z plane and the optical axis, then $y_i^{(0)}=0$. There is a matching beam expanding mirror between the dye laser and the reference cavity (see Figure 4). With respect to lens L, whose focal length is f , the object distance is a_1 and the image distance is a_4 . With respect to lens L_2 whose focal length is f_2 , the object distance is $f_1 + f_2 - a_4$ and the image distance is $-a_3$. The following equations can be obtained from the lens maker's equation:

$$\frac{1}{a_1} + \frac{1}{a_4} = \frac{1}{f}; \quad a_4 = \frac{a_1 f}{a_1 - f}$$

$$\frac{1}{f_1 + f_2 - a_4} - \frac{1}{a_3} = \frac{1}{f_1}$$

$$a_3 = \frac{f_1}{f_1} \left[\frac{f_1}{f_1} a_1 - (f_1 + f_2) \right]$$

a_3 indicates the position of the intersect between the beam from the expander and the optical axis. The angle between them is γ (γ and $\gamma' \ll 1$)

$$\gamma' = -\gamma/\beta, \beta = f_2/f_1$$

The light entering the reference cavity is equivalent to an incident beam at an angle γ' from the point S to the mirror in the reference cavity at a distance a :

$$a = a_2 + a_3 = a_2 + a_1 \cdot \beta^2 - (f_1 + f_2) \beta$$

/45

Here, the distance a , and a_2 , as well as the focal length f_1 and f_2 , are determined by the structure. By substituting γ with γ' , we get $x_1^{(0)} = a \cdot \sin \gamma'$ and $y_1^{(0)} = 0$

$$|k_{00}|^2 = \exp\left(-\frac{1}{W_0^2}((a - \bar{Z}_2)^2 + \bar{Z}_0^2) \cdot \sin^2 \gamma'\right)$$

In the example chosen above, $\bar{Z}_2 = 0$; $\sin \gamma' \approx \gamma'$ ($|\gamma'| \ll 1$). We get

$$|k_{00}|^2 = (\exp - \gamma'^2/W_0^2)$$

where

$$W_0 = \sqrt{\frac{W_0 \beta}{[a_2 + a_1 \beta^2 - (f_1 + f_2) \beta]^2 + Z_0^2}}$$

The structure used is: $f_1 = 120\text{mm}$, $f_2 = 50\text{mm}$, $\beta = 0.42$,

$$a_1 = 100\text{mm}$$
, $a_2 = 380\text{mm}$.

From these values, we get $\gamma_0 = 1.13 \times 10^{-4}$.

In case the laser beam is shifted parallelly, $x_1^{(0)} \neq 0$, $y_1^{(0)} = 0$, and $\gamma = 0$.

$$|k_{00}|^2 = \exp[-(x_1^{(0)}/W_0)^2]$$

An image is formed through the beam expander $x_1^{(0)} = \beta V$, and V is the displacement of the dye laser. We get

$$|k_{00}|^2 = \exp[-V^2/V_0^2], V_0 = W_0/\beta$$

In the above case, $V_0 = 0.391\text{ mm}$.

3. Transmittance and line width of the reference cavity

The formula for the transmittance of the resonance cavity T is:

$$T(\delta) = T_{\max} / \left[1 + \frac{4R}{(1-R)^2} \sin^2 \frac{\delta}{2} \right]$$

where $\delta = 4\pi d/\lambda$. d is the distance of the reflective mirror (including the phase change caused by the reflecting surface), λ is the wavelength, and f is the incident light frequency. When $\delta = 2\pi N$ or the path difference $2d = N\lambda$ when N is an integer, the transmittance has a maximum T_{\max} . The half width is $2\delta_H$.

$$\delta_H = 2\arcsin[(1-R)/2\sqrt{R}]$$

The corresponding frequency is f_H (see Figure 5)

$$f_H = (\delta_H/2\pi)(c/2d)$$

In this example, $R = 0.99$ and $f_H = 1.043$ MHz.

The frequency corresponding to the half width $2\delta_H$ is $2f_H = 2.086$ MHz.

4. Effect of light beam direction change on frequency stability

When the dye laser and the reference cavity are on the same incident axis, the transmission curve is $I_0 T(f)$, where I_0 is the incident light intensity. The laser frequency is stabilized at the half value point S , i.e., $I_{\text{Res}} = I_{\max}/2$. When the dye laser enters at an inclined angle, the transmission curve is $|k_{\text{ss}}|^2 \cdot I_0 T(f)$. However, the frequency is still controlled at a fixed intensity I_{Res} . Therefore, the operating point will shift from S toward S' . The dye laser frequency change Δf is

$$\Delta f = \frac{\Delta\delta}{2\pi} \cdot \frac{c}{2d}$$

From Figure 5, one can write the following formula:

$$I_{\text{Res}} = |k_{\text{ss}}|^2 I_0 T\left(N \frac{c}{2d} \mp f_H \pm \Delta f\right)$$

Hence, we get

$$|\Delta f| = f_H (1 - \sqrt{2|k_{\text{ss}}|^2 - 1})$$

The values of $\Delta f/f_H$ were calculated for various laser beam directions in the reference cavity. They were shown in Figures 6 and 7. From these figures one can see that the frequency variation has a square relationship with the change in direction. A small change in the laser direction can cause a relatively large frequency variation.

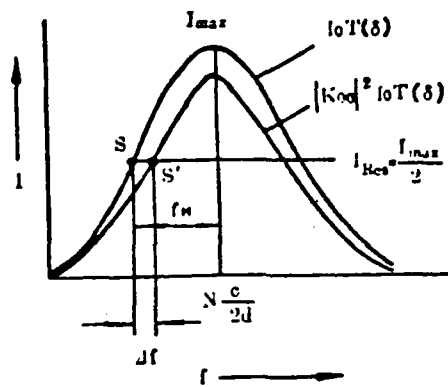


Figure 5. Effect of dye laser beam direction change on frequency stability

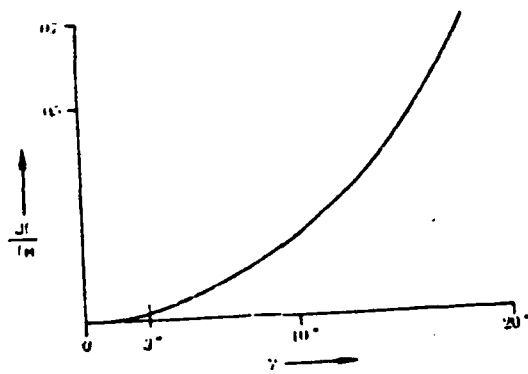


Figure 6. Dependence of ratio of frequency change to half width of resonance cavity upon direction of dye laser γ

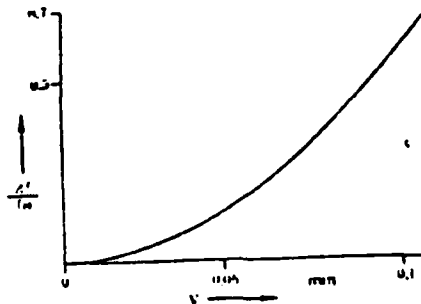


Figure 7. Dependence of ratio of frequency change to half width of resonance cavity upon displacement of dye laser beam V

1.. Interferometer for measuring beam direction change

An interferometer was designed for the sensitive measurement of the change of laser beam direction relative to the optical axis (see Figure 8). This is a modified Michelson interferometer. One of the mirrors was replaced by a symmetric reflector K (e.g., cat's eye"). An incident beam entering the interferometer at an angle γ was reflected by the reflective mirror and the "cat's eye". The angle between the two reflected light beams is 2γ (see Figure 9). The path difference between the two beams is $(N+1/4)\lambda$, which means the effective phase difference $\gamma = 2.4 \cdot 10^{-11}$. The interference pattern thus obtained varies symmetrically with the angle of inclination relative to the optical axis in the opposite direction (see Figure 9). The interference pattern was received by a quadrant photomultiplier. The normalized measurement signals in both directions are:

$$U_r = \frac{(U_A + U_D) - (U_B + U_C)}{(U_A + U_D) + (U_B + U_C)}$$

$$U_t = \frac{(U_A + U_B) - (U_C + U_D)}{(U_A + U_B) + (U_C + U_D)}$$

In order to obtain the optimal sensitivity for the interferometer, two conditions must be satisfied.

(i) The phase difference between the two reflected beams from the arms of the interferometer is $\Delta\phi = \pi/2$. This condition can be met by using a $\Delta\phi$ controller to stabilize the path difference of the interferometer to $(N + 1/4)\lambda$

(ii) The wavefront of the reflected beams from the two arms of the interferometer should have the same radius of curvature at the quadrant photomultiplier. This can be designed by the Gaussian light transmission matrix method.

2. Sensitivity and resolution of the interferometer

After a Gaussian light beam enters the interferometer, the field intensities of the two exit beams are:

$$E_1 = E_{10} \exp[-(x^2 + y^2)/W_0^2]$$

$$+ i(\omega t - k\gamma x + \phi)$$

$$E_2 = E_{20} \exp[-(x^2 + y^2)/W_0^2]$$

$$+ i(\omega t - k\gamma x + \phi - \Delta\phi)$$

where E_{10} and E_{20} are the incident field intensities, and γ is the incident angle. The total light intensity

$$B(x, y) = g |E_1 + E_2|^2$$

$$g = (1/2)(\epsilon\epsilon_0/\mu\mu_0)^{1/2}$$

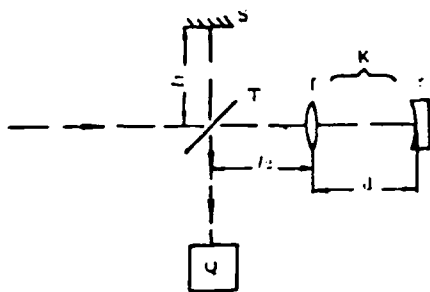


Figure 8. Interferometer for measuring dye laser direction changes.
S: reflecting mirror,
T: beam splitter,
K: cat's eye and
Q: quadrant receiver

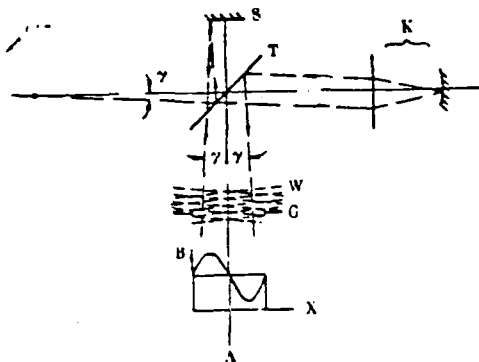


Figure 9. Formation of interference pattern at incident angle γ .
W: wave front; G: view field
A: quasi-straight optical axis.
Lower portion: light intensity distribution

The flux difference on the quadrant photomultiplier is:

$$\begin{aligned} \Delta P_s &= (P_A + P_D) - (P_B + P_C) \\ &= \int_0^a dx \int_{-\infty}^{\infty} B(x, y) dy \\ &\quad - \int_{-a}^0 dx \int_{-\infty}^{\infty} B(x, y) dy \\ &= \pi W_0^2 \cdot E_{10} E_{20} g \sin \Delta\phi \\ &\quad \times I_m \{W [\sqrt{2} \gamma / (W_0 / Z_0)]\} \end{aligned}$$

where the error function is

/47

$$W(z) = e^{-z^2} \left(1 + \frac{2z}{\sqrt{\pi}} \int_0^z e^{t^2} dt \right)$$

The sum of the flux on the quadrant photomultiplier is:

$$P_0 = P_A + P_B + P_C + P_D \\ = g w_0^2 (\pi/2) (E_{1+}^2 + E_{1-}^2)$$

The normalized optical signal of the interferometer is

$$\Delta P_x / P_0 = I_m W(\sqrt{2} \gamma Z_0 / W_0)$$

As shown in Figure 10, the curve is applicable to all Gaussian light beams.

The resolution of the interferometer is, in principle, determined by the noise of the quadrant receiver. The angular resolution γ_s is defined as the equivalent angle at which the signal current Δi of the interferometer equals the noise current i_s of the receiver.

$$i_s = (2qbi_0)^{1/2}$$

where q is the basic charge, b is the bandwidth of the receiver, and i_0 is the sum of photocurrent of the quadrant receiver.

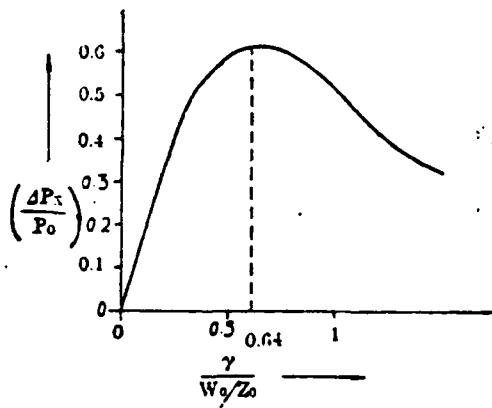


Figure 10. Dependence of the ratio of the output signal to the total power of the quadrant receiver ($\Delta P_x / P_0$) upon the parameter $\gamma / (W_0 / Z_0)$.

W_0 / Z_0 : divergence angle of dye laser

W_0 : waste radius of the dye laser on the receiver

Z_0 : $\pi \times W_0^2 / \lambda$

$$\Delta i = \frac{\eta q \lambda}{hc} P_{\text{out}} I_m \left[W \sqrt{2} \gamma Z_0 / W_0 \right]$$

where η is the quantum efficiency. By substituting $\Delta i = i_s$, we get

$$\gamma_s = \frac{1}{4W_0} \left[\frac{hc\lambda b}{\eta \pi P_{\text{out}}} \right]^{1/2}$$

According to the parameters in this example, $\gamma = 2.4 \cdot 10^{-12}$ radian. From the above formula, one can see that γ_s is inversely proportional to W_o . W_o is determined by the laser, which can be enlarged by a telescope. However, the angle γ was simultaneously reduced. Therefore, γ_s was not improved. In order to calculate the sensitivity of the interferometer, it is necessary to calculate the voltage and voltage difference of the quadrant receiver, i.e.

$$U_o = I_o R_i = U_A + U_B + U_C + U_D$$

$$\Delta U = \Delta i R_i = (U_A + U_B) - (U_C + U_D)$$

The normalized single voltage of the interferometer is

$$U_s = \frac{\Delta U}{U_o} = \frac{(U_A + U_B) - (U_C + U_D)}{(U_A + U_B) + (U_C + U_D)} 10 \text{ V}$$

$$\approx 10 I_o [W(\sqrt{2}\gamma/(W_o/Z_o))] \text{ V}$$

$$U_s \approx 10 \frac{\sqrt{2}}{\Gamma(3/2)} \frac{\gamma}{W_o/Z_o} \text{ V} \quad (\gamma/(W_o/Z_o) \ll 1)$$

The sensitivity U_s of the interferometer is not related to the intensity of the laser beam because the electronic system employs a normalized signal, i.e., the signal was obtained by dividing the voltage difference of the quadrant receiver to the voltage.

In the above example, the sensitivity of the interferometer is $0.86''/\text{volt}$.

Measurement and stability of the change in dye laser beam direction

The principle of the measuring device is shown in Figure 11. The path difference at the arms of the interferometer has stabilized at $(N + 1/4)\lambda$ by the sum of the voltage on the quadrant receiver, the phase controller and the piezoelectric ceramic on the "cat's eye" reflective mirror. The adjustable mirror S_v may be adjusted by PZT in two directions. The PZT was calibrated by a photoelectric autocollimator. When the dye laser was incident perpendicular to the reference cavity through mirrors S_v and S_2 and telescope L , a portion of the dye laser would enter the interferometer through S_1 and T_s . The interference signal was received by the quadrant receiver. The interferometer

was adjusted so that the output signal γ_x and γ_y are zero. When the dye laser beam direction changes, the output signals, γ_x and γ_y , are not zero. They are recorded by an x-y recorder or read by a digital meter. γ_x and γ_y are used as error signals to adjust the piezoelectric ceramic on the adjustable mirror S_v to make $\gamma_x = \gamma_y = 0$. The direction of the dye laser thus remains unchanged. Consequently, the effect on frequency is eliminated.

The testing results are shown in Figure 12. From the figure, one can see that the designed interferometer and servo system can stabilize the direction of the laser beam very effectively. The bandwidth of the system is 50 Hz. From Figure 12a and c, one can read the effective angular changes in the X and Y directions are $\gamma_{x,\text{eff}} = 0.13''$ and $\gamma_{y,\text{eff}} = 0.18''$. The overall effective change is $\gamma_{\text{eff}} = (\gamma_{x,\text{eff}}^2 + \gamma_{y,\text{eff}}^2)^{1/2} = 0.22''$. Considering the imaging effect of the telescope in front of the interferometer (magnifying by 14 times), $\gamma_{\text{eff}} = 3''$. The effect of this angular variation on the stability of the frequency was calculated from the formula in the previous section was calculated to be $\Delta f_{\text{eff}} = 17 \text{ KHz.}$

In addition, the dependence of the dye laser direction change on other parameters was measured. The relation between the dye laser beam direction in the horizontal direction with various dye injection pressure (or flow rate) is that the angular variation is less at high pressures (8.25 Pa) than that at low pressures (6 Pa). At a high pumping power (e.g. 6W), the angular variation is less than that at a low pumping power (4W).

In the dye laser optical path, air fluctuation has a large effect on the direction of the beam. The position of the pumping light waste on the dye flow must also be adjusted.

The flow of dye has a great effect on the stability of the dye laser. This setup can be used to test various nozzle

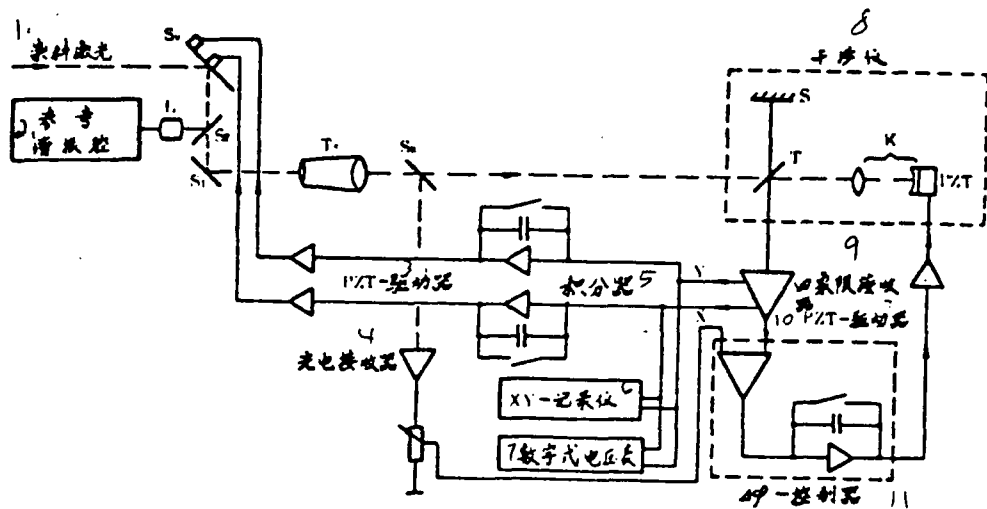


Figure 11. Stability principle of the interferometer and principle of the auto-stabilizing of dye laser beam direction.

1--dye laser; 2--reference resonance cavity; 3--PZT-driver;
4--photoelectric receiver; 5--integrator; 6--XY-recorder;
7--digital voltmeter; 8--interferometer; 9--quadrant receiver;
10--PZT driver; 11-- $\Delta\phi$ -controller

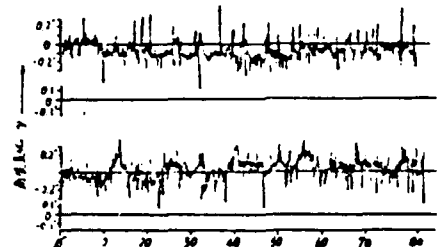


Figure 12. Dye laser direction variation in horizontal and vertical directions with time (curves a and c) and curves after using the directivity stabilizing system (b and d).

designs and the effect of other flow related parameters in order to find the optimal resolution.

References:

[1] 颜树生, PTB-Bericht, PTB-Mc-42, (1983)

- [2] D. Holwe, Appl. Opt., 18, 1632 (1979).
- [3] D. Hirlman, Opt. Lett., 3, 19 (1978).
- [4] D. Modarress, Tan Hung and S. Elghobashi, 1983, AIAA 21st Aero. Sci. Meeting Nevada.
- [5] M. Yeoman, Winter Annual Meeting of ASME, Phoenix, Nov. 14-19, (1982).

Wang Anning and Wu Nanzhan
(Chengdu Institute of Electric Welding Machines)

Monitoring atmosphere pollution by lasers has advantages such as high sensitivity, fast speed and convenience. Therefore, it attracts more and more attention. The tunable CO₂ laser has more than 40 lines in the 9.2-10.8 μm wavelength range. In this band, atmospheric pollutants, such as benzene, ammonia, butadiene, trichloroethylene and methanol, absorb strongly. Therefore, their concentrations can be measured. Here, we want primarily to introduce a simple, accurate and fast method to demarcate the wavelength of the tunable CO₂ laser.

A tunable CO₂ laser usually uses a grating as the frequency selecting element. The laser wavelength is selected by turning the grating.

We determined the source of each spectral line based on the law governing the tunable CO₂ laser in order to demarcate the wavelength. The grating diffraction formula is $\lambda_L = 2d \sin \theta$, where d is the grating constant and θ is the angle between the normal direction of the grating and the light beam.

We installed an odd calliper on one side of the grating. It was placed against the grating link. The angle θ is read by the calliper. Assuming that the distance from the rotating axis of the grating to the contact between the calliper and the link is b , then the change in the calliper reading ΔS is $b\Delta\theta$ when the variation of θ is very small (the relation between ΔS , b and $\Delta\theta$ is shown in Figure 1).

In addition $\Delta\lambda_L = 2d \cos \theta \Delta\theta$, we get

$$\Delta S = \frac{b \Delta \lambda_L}{2d \cos \theta} = \frac{-\Delta \bar{v}b}{2d \bar{v}_L \cos \theta} \quad (3)$$

where \bar{v} is the wave number. From this, one can see that the reading of the calliper varies almost linearly with wavelength

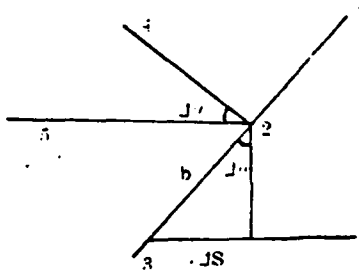


Figure 1. 1--grating; 2--grating axis; 3--contact between calliper and grating support; 4--normal direction of direction; 5--laser beam

number of the CO_2 laser spectrum is:

$$\tilde{v} = (\tilde{v}' \frac{1}{J'} - \tilde{v}'' \frac{1}{J''}) + B' J' (J' + 1) - B'' J'' (J'' + 1)$$

$$J' - J'' = \pm 1$$

1--vibration

In the P branch, $J' - J'' = J' - J = -1$. In spectroscopy, it is customary to replace J'' by J :

$$\tilde{v}_p(J) = \tilde{v}_0 + B'(J-1)J - B''J(J+1)$$

$$= \tilde{v}_0 - (B' + B'')J + (B' - B'')J^2$$

where $B \approx B' \approx B''$. When J is very small, $(B' - B'')J^2$ may be omitted. Hence, $\tilde{v}_p(J) \approx \tilde{v}_0 - 2BJ$

In the case of the transmission of CO_2 molecules in the range from $10.4 \text{ } \mu\text{m}$ to $9.4 \text{ } \mu\text{m}$, $J = 2, 4, 6 \dots$

In the R branch, $J' - J'' = J' - J = 1$. Then

$$\tilde{v}_R(J) = \tilde{v}_0 + B'(J+1)(J+2) - B''J(J+1)$$

$$= \tilde{v}_0 + (3B' - B'')J + (B' - B'')J^2 + 2B'$$

$$\approx \tilde{v}_0 + 2BJ + 2B$$

/37

where $J = 0, 2, 4, 6 \dots$ Therefore, the transition spectrum near \tilde{v}_0 , is shown in Figure 2.

\tilde{v}_0 in the figure is not allowed because the even transition from $J' = 0$ to $J'' = 0$ is forbidden. From Figure 2 one can see that the spacing between P(2) and R(0) is 1.5 times that between two neighboring lines. The spacing between P(2) and R(2) is 2.5 times. That between P(6) and R(6) is 6.5 times.

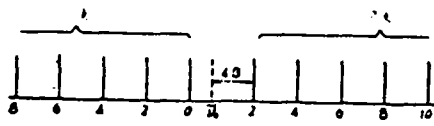


Figure 2.

(or wave number) for several neighboring wavelengths. The approximate formula for the wave

Because the gain of R(4) is higher than that of P(4), the P(6) line may appear next to the R(4) line. In this case, the spacing is 5.5 times. Therefore, it is easy to identify the spectral transition. Once we determined a spectral line, dozens of lines of the CO₂ laser could be demarcated in the 10.4 μm to 9.4 μm range based on the linearity between the calliper reading and the wavelength (or wave number). It is also possible to resolve the spectral transition.

The results of the measurements are shown in Table 1. One can see that the laser wavelength is approximately linear with the calliper reading. This indicates that this demarcation method for CO₂ laser is simple and easy and accurate. It is undoubtedly a powerful tool for monitoring atmospheric pollution.

TABLE 1. Calibration of wavelength

跃迁	波长 ² 谱线	千分尺 ³ 读数 (mm)	跃迁	波长 ⁴ 谱线	千分尺 ⁵ 读数 (mm)
P(6)	10.458	22.49	P(18)	10.571	23.63
P(8)	10.476	22.70	P(20)	10.591	23.83
P(10)	10.494	22.88	P(22)	10.611	24.04
P(12)	10.513	23.07	P(24)	10.632	24.24
P(11)	10.532	23.25	P(26)	10.653	24.45
P(16)	10.551	23.44	P(28)	10.675	24.66

1--transition line; 2--wavelength; 3--calliper reading;
4--transition line; 5--wavelength; 6--calliper reading

END

FILMED

8-85

DTIC